UNIVERSIDADE DE LISBOA
FACULDADE DE CIÊNCIAS
DEPARTAMENTO DE FÍSICA


# Graded-index fibre-based absorption spectroscopy using microfluidic devices

Kamalpreet Kaur Gill

**Mestrado Integrado em Engenharia Física**

Dissertação orientada por:
Professor David George Lancaster
Professora Guiomar Gaspar de Andrade Evans

2021

*“Great things are not done by one person. They’re done by a team of people.”*

- Steve Jobs

*“Success is a journey not a destination. The doing is usually more important than the outcome.”*

- Arthur Robert Ashe, Jr.

# Acknowledgments

This thesis report is the result of the work that I performed at the facilities of the Future Industries Institute, University of South Australia. During my one-year placement, I did the practical work, a detailed description of the activities of the same is provided in this thesis report. In 2019, I hesitated to accept this internship opportunity in Australia, but in retrospect this was definitely one of the best decisions in my life and I would not miss a single day! In Laser Physics and Photonic Devices (LPPD) laboratories I found a very inspiring environment, something that contributed to enrich my scientific and social experiences.

First of all, I am grateful to the University of South Australia for giving me the opportunity to make my internship in such a great place. Then, I would like to thank more specifically my supervisors in Australia, Dr. Nicolas Riesen, Professor David Lancaster and Professor Craig Priest, for their support throughout this work and the time they took for me. I really appreciate them for providing a lab with excellent infrastructure, and for providing me the opportunity to publish this research at an international platform. Additionally, I would like to address a special thanks to Dr. Nicolas Riesen for his endless support, encouragement and help to complete this thesis. Also, I am cordially grateful to Dr. Bin Guan for guiding me to prepare the samples for my experiments.

I and my supervisors mentioned above, acknowledge financial support from ULVAC Inc., and the Australian Research Council Integrated Devices for End-User Analysis at Low Levels Research (IDEAL) Hub (IH150100028).

I must also express my gratitude to Nicholas Phillips for his essential support for GIF fibers and for all the scientific discussions to find the best parameters that fulfill requirements of my project. Furthermore, I would like to thank my supervisor at the University of Lisbon, Professor Guiomar Evans for her availability and her valuable advice. Similarly, I would like to thank my office mate Dr Mamoona Khalid for her precious inputs. A big thanks for all the time we spent together experimenting, sharing ideas and experiences.

Finally, I am thankful to my parents and my brother for providing me necessary mental support and making this study possible, even if being physically at the other end of the world. I would also like to thank all the staff members of LPPD group and ARC Research Hub members who helped me while conducting this work. It was pleasure to work with all these wonderful personalities and motivated colloborators. I sincerely thank everyone for contributing to make my journey unforgettable in Australia.

# Publications


**1.** K. K. Gill, N. Riesen, C. Priest, N. Phillips, B. Guan, and D. G. Lancaster, "On-chip absorption spectroscopy enabled by graded index fiber tips," *Biomedical Optics Express,* vol. 12, no. 1, pp. 181-190, 2021.

**2.** N. Riesen, K. Gill, C. Priest, N. Phillips, B. Guan, and D. G. Lancaster, "Graded-index fiber on-chip absorption spectroscopy," presented at the CLEO Laser Science to Photonic Applications 2021, Conference Paper.

# Abstract

In recent years, increasing efforts of developing novel micro and nano technologies have been dedicated to improve human health. These advances in the field of nanotechnology have facilitated the development of miniaturized microfluidic lab-on-a-chip (LOC) devices, which are frequently described as miniature versions of their macro-scale counterparts. Microfluidic LOC devices present great benefits in terms of small sample volumes and fast analysis times. From an optical point of view, these devices still suffer a drastic reduction in the optical pathlength compared to macroscale experiments. Obviously the reduced optical pathlength complicates or reduces the effectiveness of the application of various optical techniques in lab-on-a-chip systems. Meanwhile these devices are gaining a broader acceptance in clinical medicine for disease diagnosis.

This thesis describes the recent work performed in the field of optofluidics with the application of optical sensing systems for microfluidic devices. Optofluidics is a combination of optics/photonics and microfluidics field. In optofluidic devices the micro-photonic components are integrated on microfluidic devices, which are able to hold the fluids at the microlitre scale. Optofluidic devices are used to perform interactions between light and fluids at micro scale level for applications in physics, chemistry and biology. These chip-scale devices could be easily integrated into a LOC system that is a compact platform and does not require free-space optics to perform laser-based spectroscopy, such as absorption spectroscopy. Absorption spectroscopy (AS) is a powerful technique for studies of species (atoms and molecules) and detection of unknown concentrations. The spectroscopic analysis is not only applied in physics and chemistry but also in biology and medicine [1]. Although a large number of molecular species can successfully be detected with established AS techniques, there are some applications that require higher sensitivity, selectivity and accuracy, yet robust and compact instrumentation.

In this work, a LOC device was developed based on the optofluidics concept. The relevance of integration of micro-optical components in an "on-chip" approach is compared with the "off-chip" approach which was coupled with macro-scale optical infrastructure. The design and characterization of miniaturized optofluidic devices for sensing based on integrating collimating optical fibers with custom microfluidic chips is presented. The usage of graded-index (GRIN) fiber tips or GIF tips is to develop a compact device which does not require free space optics and the collection efficiency of GRIN fiber tips is significantly higher compared to standard single-mode fiber. The absorption spectroscopy on-chip is performed with both GIF tips and SMF configurations. To compare the performance of both fibres, the beam divergence and the insertion losses were measured. The reduction in both beam divergence and insertion losses for the GIF configuration compared with SMF were found to be 4-fold, for a 10 mm channel. Absorption spectroscopy was demonstrated on chip for the measurement of red colour dye (Ponceau 4R) and the detection of thiocyanate (SCN) which is an indicator of oral health and a detoxification product of cancer treatments. The thiocyanate concentrations were detected in water and also in a complex biofluid i.e. artificial human saliva.

The proposed optofluidic setup allows for absorption spectroscopy measurements to be performed with only 200 $\mu L$ of solution which is an order of magnitude smaller than for standard cuvettes but provides comparable sensitivity. To assess the performance of the miniaturized device, the absorption measurements

are also compared with a standard cuvette of the same pathlength (~10 *mm*). A quantitative comparison of both devices demonstrates the consistency of linearity of absorbance against the concentration of analyte, accordingly to the Beer-Lambert law. The demonstrated approach has the potential to be used for chemical and biochemical analysis of DNA, proteins or saliva where the use of small volumes is critical.

In order to perform spectroscopic analysis of human body proteins, a new sensing device was developed using a compacted chip with micropillar arrays called "Pillar Cuvette (PC)". The PCs are fabricated at ANFF-SA (Australian National Fabrication Facility - South Australia Node). The design and fabrication process of PCs is briefly presented in this thesis. The CLIC3-HIS tag protein (human body protein) and BSA protein (Bovine protein) spectroscopic analysis were performed in UV range of spectrum. We developed a new approach to optical manipulation of excitation fibre and collection fiber setup. The proposed design and setup are presented in which optical fibers and the PC are integrated directly on a compact platform that doesn't require alignment. It is an integrated pre-aligned device which is wholly portable.

# Keywords

Lab-on-a-chip, Optical Detection, Integrated optics, Optofluidics, spectroscopy

# Resumo

Nos últimos anos, os esforços crescentes de desenvolvimento das novas tecnologias têm-se dedicado a melhorar a saúde humana. Esses avanços no campo da nanotecnologia facilitaram o desenvolvimento de dispositivos microfluídicos, designados *lab-on-a-chip* (LOC), que são frequentemente descritos como versões em miniatura de seus equivalentes em macro escala. A área dos microfluídicos trata dos fluidos em escala micrométrica para fins de controlo de fluxo ou deteção das espécies químicas. Os dispositivos microfluídicos apresentam grandes vantagens, incluindo consumo mínimo de volumes de amostra, tempos de análise rápidos e custo de fabricação reduzido [2]. Com o avanço nas tecnologias de fabricação, as áreas de ótica e da fotónica também se adaptaram para desenvolver componentes óticos na micro e nano escala. A pesquisa na escala micrométrica deu origem a outro tópico chamado opto-fluídos. A área de opto-fluídos é muito recente, surgiu apenas no início de ano 2000 e a pesquisa neste tópico está crescendo exponencialmente de um ano para o outro [3]. A área de opto-fluídos estuda a interação entre fluído e luz, aproveitando a tecnologia existente nas áreas de microfluídicos da ótica. Os dispositivos opto-fluídos são geralmente baseados na integração de tecnologias óticas/fotónicas no dispositivo microfluídico. Do ponto de vista ótico, os dispositivos opto-fluídos sofrem uma redução drástica no comprimento do caminho ótico, em comparação com os instrumentos em macro escala. Obviamente, o comprimento do caminho ótico reduzido complica ou traz problemas na utilização de técnicas de deteção e isso, por sua vez, reduz a eficácia das técnicas óticas em sistemas LOC. Enquanto isso, esses dispositivos estão a ganhar aceitação crescente no campo da medicina clínica para o diagnóstico de várias doenças.

A presente tese descreve o trabalho recente realizado na área de opto-fluídos, utilizando um sistema de sensores óticos num dispositivo microfluídico. Os dispositivos opto-fluídicos são usados para realizar interações entre luz e fluídos em nível de microescala para aplicações em física, química e biologia. Os componentes óticos ao nível de escala de um *micro-chip* podem ser facilmente integrados em um sistema LOC que também é uma plataforma compacta. Deste modo, os sistemas opto-fluídos não requerem ótica de espaço livre para realizar espectroscopia baseada em laser, como a espectroscopia de absorção. A espectroscopia de absorção é uma técnica poderosa para estudos de espécies (átomos e moléculas) e deteção de concentrações desconhecidas. Embora um grande número de espécies moleculares possa ser detetado com sucesso através das várias técnicas estabelecidas de espectroscopia, existem algumas aplicações que requerem maior sensibilidade, precisão e instrumentação mais robusta e compacta.

Neste trabalho pretendeu-se desenvolver um dispositivo LOC com base no conceito de opto-fluídos. A espectroscopia de absorção foi demonstrada no dispositivo compacto e miniaturizado (LOC) desenvolvido usando fibras que têm pontas de índice graduado (GRIN) que também são conhecidas por pontas GIF. Essas fibras permitem desenvolver um *lab-on-a-chip* altamente eficaz que é compacto, conectada por fibra e que não requer ótica de espaço livre para criar o caminho ótico. A espectroscopia de absorção no chip é realizada com duas configurações, ou seja, pontas GIF e SMF. Para comparar o desempenho de ambas as fibras, a divergência do feixe e as perdas de inserção foram medidas. A eficiência de coleção do feixe na ponta de fibra GRIN (125 $\mu m$) é significativamente maior em comparação com a fibra de modo único - SMF (125 $\mu m$). As pontas GIF têm o feixe colimado na saída da fibra que é transmitida longitudinalmente através de um microcanal e que é coletada por uma fibra multi-modo na outra extremidade do microcanal. Desta forma, fabricamos um dispositivo opto-fluídico que permite melhorias significativas no aumento do

comprimento de interação, para espectroscopia de absorção de passagem única, usando pontas de fibra de índice graduado (GIF).

A relevância da integração de componentes micro-óticos na abordagem *on-chip* é comparada com a abordagem *off- chip*, que foi acoplada à infraestrutura ótica em macro escala. A configuração opto-fluídica proposta permite que as medições de espectroscopia de absorção sejam realizadas com apenas 200 µL de solução, que é uma ordem de magnitude menor do que as efetuadas com uma cuvete padrão (3.5 *mL*), mas que fornece sensibilidade comparável. Para avaliar o desempenho do dispositivo miniaturizado, as medições de absorção também são comparadas com uma cuvete padrão do mesmo caminho ótico (~10 mm).

A espectroscopia de absorção foi demonstrada em 3 configurações (cuvete padrão; dispositivo opto-fluídico com fibra SMF; dispositivo opto-fluídico com fibra GIF) para a medição do corante vermelho (Ponceau 4R). Para demonstrar ainda mais o uso do dispositivo opto-fluídico, mostramos que esse pode ser usado para a deteção de analitos biologicamente relevantes, como o *thiocyanate* (SCN). O SCN foi escolhido porque é um produto usado na desintoxicação de fármacos utilizados no tratamento do cancro e é um indicador de saúde bucal, incluindo a exposição ao fumo passivo que pode aumentar significativamente as concentrações de SCN para níveis potencialmente capazes de afetar a glândula tireoide. Numa comparação quantitativa, o dispositivo demonstrou a consistência da linearidade da absorbância em relação à concentração do analito, de acordo com a lei de Beer-Lambert Também exploramos a configuração opto-fluídica com a ponta GIF para deteção de SCN em uma matriz de uma amostra mais complicada (que não é apenas água) a saliva humana artificial. Reforçando assim, o estudo do potencial deste dispositivo para diagnóstico de amostras complexas. A abordagem demonstrada mostrou ter potencial para ser usada para análises químicas e bioquímicas de ADN, proteínas ou saliva onde o uso de pequenos volumes é crítico. De modo a fazer comparação entre duas fibras, foram efetuados estudos de feixe de divergência ao longo de microcanal e as perdas de inserção entre a fibra de excitação (GIF) e a fibra de coleção (MMF). Foi obtida uma redução 4 vezes inferior na divergência do feixe e nas perdas de inserção para a configuração GIF em comparação com SMF, para um canal de 10 mm de comprimento.

O trabalho foi complementado com a análise espectroscópica das proteínas do corpo humano. Para tal, foi utilizado um *chip* compactado com matrizes de micropilares denominado *Pillar Cuvette* ou PC. Os PC foram fabricados na ANFF- SA (Australian National Fabrication Facility - South Australia Node). O processo de desenho e fabricação do PC é brevemente apresentado neste trabalho. A análise espectroscópica da proteína CLIC3-HIS *tag* (proteína do corpo humano) e da proteína BSA (proteína bovina) foi realizada na faixa de espectro do ultravioleta (UV). Utilizando os métodos prévios não foi possível determinar o pico de absorvância esperado a $\lambda$=280 nm. Face a este resultado, foi desenvolvido um novo dispositivo opto-fluídico que tem alta viabilidade de integração na plataforma *lab-on-a-chip*. Neste novo dispositivo as pontas GIF são configuradas num PC. Na nova configuração desenvolvida, o feixe é transmitido através da secção transversal do PC, permitindo aumentar o comprimento do caminho ótico mantendo 2 µL - 3 µL de volume de amostra.

Para futuro trabalho, o desenho de uma plataforma foi desenvolvido para integração compacta dos PC e das ambas as fibras. Esta nova plataforma está em processo de fabricação e será testado nas futuras experiências. Um bom resultado nos testes permitirá alargar o universo de utilização destes dispositivos em análises químicas e bioquímicas com volume de amostra e tempo de análise reduzido. Deste modo, a crescente

disponibilidade de ferramentas e técnicas na indústria de nanotecnologia vai fornecer um caminho para trazer essas inovações do laboratório para a vida cotidiana.

# Palavras-Chave

Lab-on-a-chip (laboratório num chip),  Deteção ótica, Ótica integrada, Opto-fluídos,, Espectroscopia

# Contents


Acknowledgments ..... 4
Publications ..... 5
Abstract ..... 6
Keywords ..... 8
Resumo ..... 9
Palavras-Chave ..... 12
Contents ..... 13
List of Figures ..... 15
Acronyms ..... 18
Chapter 1 Introduction to Optofluidics ..... 19
1.1. Motivation ..... 20
1.2. Objectives ..... 20
1.3. Overview of the Dissertation ..... 21
Chapter 2 Optofluidic Devices ..... 22
2.1 Absorption Spectroscopy with Optofluidic Devices ..... 23
2.2 Optical Fibres: Graded-index Fibres ..... 25
2.3. Our Approach ..... 28
Chapter 3 Optofluidic Device Based on Graded-index Fibres ..... 30
3.1. Device Design and Fabrication ..... 30
3.1.1. Integrated Optical Fibres ..... 31
3.1.2. Absorption Spectroscopy Experimental Setup ..... 34
Chapter 4 Experimental Results and Discussion ..... 39
4.1. Red Colour Food Dye ..... 39
4.2. Fibre characterization ..... 41
4.3. Iron (III) Thiocyanate $[\mathbf{FeSCN2}+]$ in Water ..... 46
4.4. Iron Thiocyanate $[\mathbf{FeSCN2}+]$ in Artificial Saliva ..... 49
Chapter 5 Pillar Cuvette ..... 51
5.1. Pillar Cuvette Fabrication ..... 52
5.2. Absorption Spectroscopy Using the Pillar Cuvette ..... 53

5.3. Cross-section Pillar Cuvette Absorption Spectroscopy ..... 58
5.3.1. Proposed Solutions – Pillar Cuvette Holder ..... 60
Chapter 6 Conclusions ..... 62
References ..... 64
Journal article ..... 67

# List of Figures

**Figure 1**. Schematic of an ideal all-optofluidic system for lab-on-chip applications. Image adapted from [12]. ..... 22

**Figure 2.** The basic setup to perform absorption spectroscopy with an optofluidic device. A beam of light passes through a liquid core (microchannel) containing the absorber with concentration (c). At the other end, the output signal is measured by a suitable detector. Image adapted from [12]. ..... 23

**Figure 3.** Energy diagram showing the absorption of a photon by an atom or a molecule of a chemical analyte. Image adapted from [13]. ..... 24

**Figure 4.** Structure of an optical fibre. Image adapted from [22]. ..... 26

**Figure 5.** Propagation of light rays through an optical fibre. Image adapted from [23]. ..... 26

**Figure 6.** Schematic of GIF tip composed of a single-mode fibre spliced to a mode expanding coreless fibre, which is spliced to a graded-index fibre. ..... 27

**Figure 7**. The ray trajectory and refractive index distribution of a multi-mode step index fibre and a multi-mode graded-index fibre with parabolic index distribution. Image adapted from [22]. ..... 28

**Figure 8**. Optofluidic device based on glass slides. ..... 30

**Figure 9.** (a) Device Solidworks design showing microfluidic channel and GIF tip aligned to MMF within v-grooves (b). Close-up of microfluidic channel. ..... 31

**Figure 10.** Microscope image of GIF tip with three spliced sections identified as SMF, CF and GRIN. The measured length of CF (200 μm) and GRIN (91.74 μm). The fibre diameter is 128μm. ..... 32

**Figure 11.** Refractive index profile of single-mode fibre (SMF28), coreless fibre and GRIN fibre measured at 532nm. ..... 33

**Figure 12.** Contour plot of far-field divergence angle of GIF tips (in degrees) as a function of coreless and graded-index fibre segment lengths at $\lambda = 532$ nm. ..... 34

**Figure 13.** Experimental setup for absorption measurements with (a) standard cuvette and (b) microfluidic device. ..... 35

**Figure 14.** Schematic diagram of supercontinuum laser with internal lens and an external lens to focus the collimated beam. ..... 36

**Figure 15.** Photo of setup for standard cuvette measurements. SC: Supercontinuum Laser, MMF: Multi-mode fibre. ..... 37

**Figure 16.** Image of device filled with red food colour dye sample for a) standard cuvette setup and b) optofluidic setup..... 37

**Figure 17.** Relationship between absorbance and wavelength for red food colour concentration ranging from 5.45 µmol/L - 32.7 µmol/L. The absorbance spectrum obtained through spectrometer and using a standard cuvette with optical pathlength of 10 mm. ..... 40

**Figure 18.** Plot of absorbance at $\lambda max = 501\ nm$ of red color dye for a standard cuvette and the optofluidics chip with either GIF tip or SMF fibre, where the linear regression is A = 0.029*c according to Eq. (2). ..... 40

**Figure 19.** Illustration diagram of output power at the MMF according to the power at the end of SMF and GIF. ..... 41

**Figure 20.** Schematic representation of the beam profile measurement setup. The fibre was positioned by a 3-axis translation stage and aligned with the input aperture of the Spiricon CCD Camera detector. ..... 42

**Figure 21.** The 2D beam profile of a) GIF with coreless segment ~ 200 µm and GRIN segment ~ 100 µm; b) SMF modal nature. The beam profile is measured with Spiricon CCD camera at 0.8 mm distance from the end-face of fibre. ..... 43

**Figure 22.** Measured beam radius of SMF28 (blue curves) and GIF tip (red curves) as a function of propagation distance at 532 nm and 650 nm..... 43

**Figure 23.** The beam divergence of SMF28 and the GIF fibre (CF = 218 µm and GRIN = 91 µm) as a function of their beam propagation. The values are calculated using the data plotted in Fig. 22. ..... 44

**Figure 24.** Schematic representation of the insertion loss measurement setup. The MMF fibre was positioned on a 3-axis translation stage and aligned with the excitation fibre (GIF/SMF). The MMF fibre is moved in z axis over the 10 mm distance from end-face of excitation fibre. ..... 45

**Figure 25.** Measured insertion losses of GIF-MMF and SMF-MMF configurations. ..... 46

**Figure 26.** Relationship between absorbance and wavelength for $Fe(SCN)2+$concentration ranging from 105 µmol/L - 420 µmol/L. The absorbance spectrum obtained through spectrometer and using a standard cuvette with optical pathlength of 10 mm. ..... 47

**Figure 27.** Plot of absorbance at 480 nm for $Fe(SCN)2+$solution as a function of $SCN-$ concentration in water for standard cuvette (A = 0.0025C) and for the microfluidic chip with either GIF (A = 0.0026C) or SMF (A = 0.0024C). ..... 48

**Figure 28.** Plot of absorbance at 480 nm as a function of SCN solution in artificial saliva (A = 0.0025C) and in water (A = 0.0026C) for the GIF setup. ..... 49

**Figure 29.** 3D schematic design of a pillar cuvette with sample loading area and analysis area covered with micro-scale pillars, fabricated at University of South Australia. Note that the pillar size and the device size is not to scale. ..... 51

**Figure 30.** Schematic diagram of micropillar fabrication by UV-lithography. a) UV-exposure of substrate coated with thin chromium layer and spin-coated photoresist, through a photomask. b) The UV-exposed area changes in chemical properties of photoresist. c) Unwanted photoresist (unexposed areas) is removed by washing it with Piranha solution. d) Plasma etching of chromium layer. ..... 52

**Figure 31.** Scanning electron microscope (SEM) image of micropillars with side view. ..... 53

**Figure 32.** Schematic of experimental setup used to perform absorption spectroscopy with Pillar cuvette. The image shows the side view of pillars whose base is illuminated by the light source. Image adapted from [42]. ..... 54

**Figure 33.** The absorption of amino acid tryptophan and tryosine with their chemical structure respectively. Image adapted from [46]. ..... 54

**Figure 34.** Absorption spectrum of CLIC3-HIS protein measured using pillar cuvette with optical pathlength of 50 μm. The absorption peak at 210 nm (black dashed line) and no absorption peak observed around 280 nm (grey dashed circle). ..... 55

**Figure 35.** Absorbance measured at wavelength 210 nm over the concentration ranging from 0.123 mg/mL to 1.85 mg/mL. ..... 56

**Figure 36.** Absorption spectrum of BSA protein with optical pathlength of 50 μm using a pillar cuvette. ..... 57

**Figure 37.** Plot of absorbance at a wavelength of 280 nm against the a) concentration and b) product of pillar cuvette pathlength and concentration of BSA protein. ..... 58

**Figure 38.** Pillar cuvette with fibres placed in cross section. ..... 59

**Figure 39.** a) The alignment of GIF fibre with pillar cuvette cross-section. b) Pillar cuvette filled with liquid solution. c) Side view of pillar cuvette to represent the fibre alignment with pillars. ..... 59

**Figure 40.** Solidworks designs of stainless-steel holder for a) pillar cuvette integrated with collection fibre b) pillar cuvette integrated with GIF and MMF fibre on same platform and c) the fibre groove design and topography ..... 60

# Acronyms

GIF – graded-index fibre

MMF – multi-mode fibre

SMF – single-mode fibre

LOC – lab-on-a-chip

LOD – limit of detection

GRIN – graded-index

CEAS – cavity-enhanced absorption spectroscopy

CRDS – cavity ring-down spectroscopy

OCT – optical coherence tomography

CF – coreless fibre

MEMs – micro-electromechanical system

# Chapter 1

# Introduction to Optofluidics

In this chapter, a brief description to the optofluidics topic is provided to introduce necessary knowledge and literature to summarise the current state of the art. Sections 1.1, 1.2 and 1.3 are devoted to describe the motivation and objective, and the preview of the thesis respectively.

Optofluidics is a very young field that emerged in the early 2000's and the research in this topic is growing exponentially each year [3]. Optofluidics refers to the discipline that studies the interaction between fluid and light by taking advantage of both microfluidics and the optics field. Optofluidic devices are generally based on the integration of optical/photonic technologies within microfluidic device.

The initial concept of integrated microfluidic device was developed by Manz *et al.* in 1990 [4]. The advances over the last few decades in the field of nanotechnologies have facilitated the development of microfluidic devices with the goal of creating a laboratory on a single chip called micro-total analysis system (μTAS) or "lab-on-a-chip" (LOC). LOC devices have demonstrated great potential to perform analysis of complex biological and chemical samples for several applications such as biotechnology, chemical sensing and as a disease diagnostics platform that can be used in remote areas worldwide. Microfluidic devices are described as miniature versions of their macro-scale counterparts [5]. The miniaturized platforms present several advantages in term of consumption of small amount of sample and fast analysis which means the sample doesn't require pre-processing for example for preparing diluted solutions.

It is worth underlining that these miniaturized devices have microchannels which are generally fabricated at the micro or nano scale e.g. having at least one cross-sectional dimension in the range from about 0.1 μm to about 500 μm and they flow liquid through the device [6]. The basic idea for fabricating microfluidic chips originated from silicon chips used in the semiconductor industry in which several electronic components are printed or etched on a substrate or thin film. The most commonly used substrates in these devices are silicon, glass or polymer. There are several techniques used in the fabrication process of μTAS including UV-photolithography and etching which will be discussed later in detail in this thesis.

The opto-microfluidic devices are developed using prominent fabrication techniques to integrate several optical functions into a single chip in the lab-on-a-chip approach, replacing the need for bulk free-space optics [7]. The microfluidic devices require additional sources and detectors to perform the experiments so, they can only be used to perform analysis in laboratory experiments. The unique capability of optofluidic devices involves the simultaneous control of fluids and optical beams, which are responsible for carrying the information for further analysis. The detailed functional operations of optofluidic devices will be discussed in the next chapter. The combination of these two fields, optics and microfluidics, has attracted significant attention and many promising approaches have been undertaken to develop optofluidic devices. Despite all this development, the optofluidics field still requires new ideas in research that can create easy-to-use optofluidic devices for point-care analysis [3].

## 1.1. Motivation

One of the biggest challenges in today's world is to develop the technologies and instruments that can improve the health and lifestyle of people. Advances in the field of nanotechnology have facilitated the development of miniaturized devices called lab-on-a-chip (LOC) which are cost effective and can be used by non-specialists for health purposes such as monitoring and diagnostics of diseases. The use of LOC devices in remote settings has been perceived as potentially one of the most powerful applications of the technology by taking advantage of its small size and their benefit in small sample volume consumption.

The realization of miniaturized optofluidic platforms offers potential for achieving more functional and compact devices. Such integrated systems bring fluid and light together and exploit their microscale interaction for a large variety of applications. The high sensitivity of compact photonic devices can generate effective microfluidic sensors, with integration capabilities.

In this context, several microfluidic devices with integrated optical components have previously been developed to perform absorption, fluorescence and Raman spectroscopy [8, 9]. However, these techniques used standard optical fibres with large beam divergence, which makes it difficult to achieve high sensitivity, and it decreases the efficiency of the device. The research presented in this thesis aims to develop a compact optical detection platform for absorption spectroscopy, by integrating collimating fibres called lensed graded-index (GRIN) optical fibres tips.

## 1.2. Objectives

From the discussion above, current microfluidic devices based on photonic components are limited to small optical pathlength in single-pass absorption spectroscopy. Therefore, the main objective of this thesis is to develop optofluidic device by using graded-index fibre (GRIN) which minimizes the optical losses and increase the capability of optofluidic device to achieve longer pathlength. The specific objectives are:

1. Design and fabrication of a microfluidic device with integrated lensed optical fibres.

2. Perform absorption spectroscopy on biological samples to show the relevance of the optofluidic device.

3. Perform characterization of the newly developed optofluidic device with GIF fibre in comparison with standard single-mode fibre (SMF).

4. Perform spectroscopic measurements on compact and multichannel device which is an interchangeable chip (Pillar cuvette).

## 1.3. Overview of the Dissertation

This thesis describes the work performed at the University of South Australia for 11 months and it is divided into seven chapters. The content presented in this thesis focuses on the development of optofluidic devices with novel photonic components. The spectroscopic analyses are carried out in order to demonstrate the application of the devices for health monitoring.

The contents of the thesis are arranged as follows: Chapter 2 focuses on the principle of the optofluidics concept and its development within the microfluidic field. A detailed description of the functional operation of optofluidic device is provided alongside the other instrumentation used to perform the spectroscopy with these devices. Absorption spectroscopy and the physics behind this optical technique, i.e., absorbance of light, is explained. A brief review of the other advanced methods used in absorption spectroscopy to improve the sensitivity of device is provided for further studies. The properties of fibres are presented and the process to develop micro-lens using graded-index fibres are explained.

Chapter 3 focuses on the design and fabrication of one of the proposed optofluidic devices, in accordance with the absorption spectroscopy setup. The details are provided on the selected components for fabrication, and device demonstration with components embedded shown through a design. The experimental method to perform absorption spectroscopy with the optofluidic device and with standard cuvette is described in detail.

Chapter 4 presents the spectroscopic results obtained with red colour food dye as a test sample. The thiocyanate in water and in artificial saliva is tested to prove the ability of the device to detect biologically relevant samples. The results are compared between off-chip approach (standard cuvette) and on-chip approach (optofluidic device). Furthermore, the direct comparison between the optofluidic device using GIF and SMF is performed. To describe the difference between GIF and SMF the beam profile and the coupling losses between the excitation and collection fibre are measured.

In Chapter 5, pillar cuvette design and fabrication process are explained. The new experimental configuration with pillar cuvette is described to increase the optical pathlength for single pass absorption spectroscopy. The alignment challenges and proposed solutions are presented. Finally, CLIC3-HIS protein and BSA protein measurement results with pillar cuvette are presented. The conclusions and future work are summarized in Chapter 6.

# Chapter 2

# Optofluidic Devices

Typically, optofluidic devices are fabricated using similar techniques used in microfluidic device fabrication. Ideally all the components, e.g., optical components and microfluidic channels are embedded on a monolithic platform by using microfabrication techniques. Photonic components such as fibres or waveguides are implemented to deliver light from the source and to collect signal from microfluidic channels [10]. Fig. 1 represents a schematic of a simple optofluidic device with light going through a microfluidic channel and collected on the other side after interaction with a sample. This is very similar to conventional Micro Electro-Mechanical systems (MEMS) in which the signal is carried out by an electron instead of light [11]. The optofluidic devices offer several sensing applications in the field of solar energy, biodefense, chemical sensing, health monitoring and biomedical research [3].

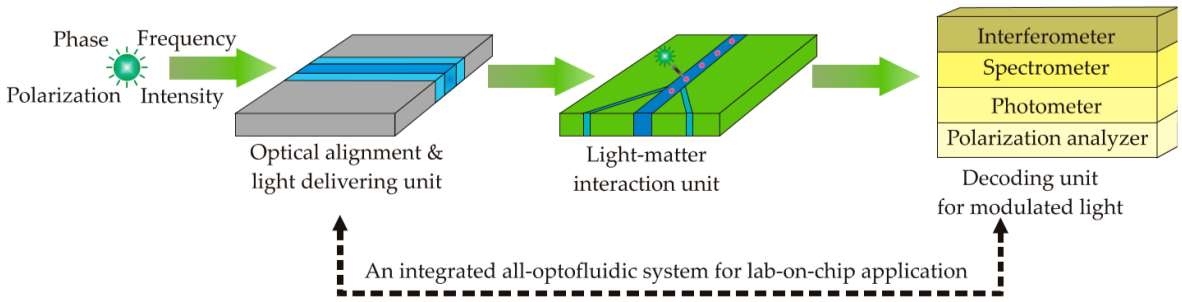


**Figure 1**. Schematic of an ideal all-optofluidic system for lab-on-chip applications. Image adapted from [12].

One of the most important issues of these devices is the miniaturization of the detection system which requires increased integration not only of fluidic elements, but also of optical elements such as fibres and lenses. However, in recent years advances in fabrication techniques have been overcome to develop suitable combination of materials for optics to integrate into microfluidic device to make these systems portable for use in non-laboratory environments. The integration of optics components on a microchip can also reduce the fabrication cost [12]. One of this thesis' main focus points is the miniaturization of optical component i.e. optical fibre integration into in-house built microfluidic device.

Absorption spectroscopy is an important optical tools which has been widely implemented on optofluidic devices [9]. The figure below presents the basic functional operation of an optofluidic device which enables light–matter interaction to achieve maximum sensitivity by offering a way to transmit the light and analytes along the same guide [12]. This method of detection is called "the on-chip approach". The experiments

conducted in this thesis research uses absorption the spectroscopy technique on both on-chip approach and off-chip approach to detect biochemicals in biofluids.

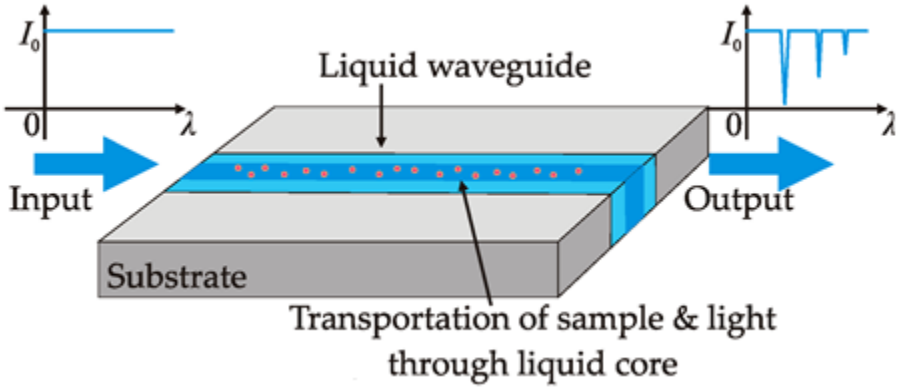


**Figure 2.** The basic setup to perform absorption spectroscopy with an optofluidic device. A beam of light passes through a liquid core (microchannel) containing the absorber with concentration (c). At the other end, the output signal is measured by a suitable detector. Image adapted from [12].

Since most lab-on-a-chip optofluidic devices have been limited to the laboratory rather than being directly integrated into user-friendly real-world products, there is a need to focus on simple, practical and cost-effective devices which balance design and real-world impact. This improves the commercial potential of techniques and technologies that are currently in development. In order to get a commercialized device some issues must be solved from the technological point of view, such as easy and simple fabrication process.

## 2.1 Absorption Spectroscopy with Optofluidic Devices

Optical spectroscopy has been used for centuries to measure the intensity of absorption, fluorescence, reflectance and scattering of radiation by liquid or solid samples. Over the past years, absorption spectroscopy has received a large amount of attention due to its growing relevance for research in applications related to micro and macro scales. Absorption spectroscopy is a well-established tool, and it is the most widely used technique for the analysis of the chemical composition of materials and for research into biological problems. The quantitative analysis of the spectrum of radiation that interacts with samples of chemical species allows the determination of concentration of unknown species present in the sample. Absorption spectroscopy is a process that relies on the absorption of light which passes through the sample. The radiation is composed by photons which are quantified in energy packets. The energy of a photon is related to its wavelength (λ) and the relation can be expressed as:

$$E = \frac{hc}{\lambda} \qquad (1)$$

where $h$ is the Plank's constant, and $c$ is the velocity of light. When the sample is exposed to light, the photon energy is absorbed by electrons of molecules/atoms of liquid. The photon radiation is quantified, and it is equal to the energy difference between the highest energy state (excited state) and the lower energy state (it can be ground state). Fig. 3 shows the diagram of energy levels, the electrons require quantized energy of photons to transfer to excited states [13].

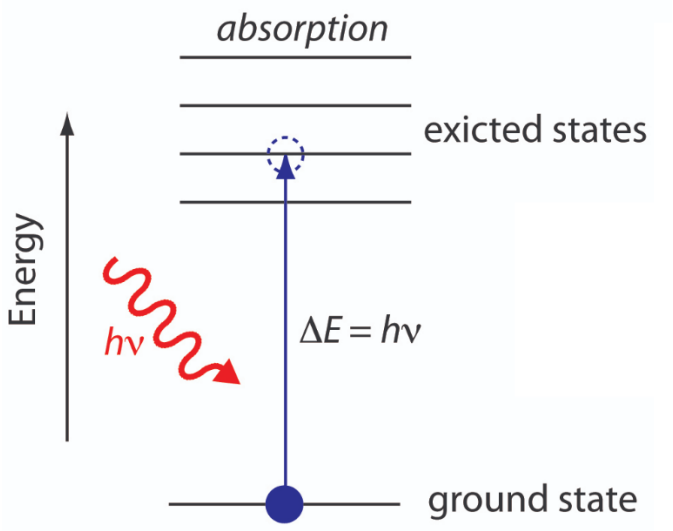


**Figure 3.** Energy diagram showing the absorption of a photon by an atom or a molecule of a chemical analyte. Image adapted from [13].

The amount of light that is absorbed by the solution depends on the concentration, the path length of the light through the liquid sample and on the molar absorptivity $\varepsilon$. The relation between the absorbed light and concentration is given by Beer-Lambert Law [14], which can be expressed by equation (2):

$$A = -\log\left(\frac{I}{I_0}\right) = \varepsilon l c \qquad (2)$$

where $I$ and $I_0$ are the intensities of light transmitted in presence and absence of an analyte, $\varepsilon$ is the molar absorptivity coefficient, $l$ is the optical pathlength and $c$ is the concentration of the analyte in the sample. As mentioned above, one of the simpler and more practical on-chip sensing techniques is absorption spectroscopy which can be used to determine the concentration of an analyte of interest through the Beer-Lambert Law.

Miniaturized devices present great benefits in terms of small sample volumes and fast analysis time. From an optical point of view, miniaturized devices however suffer a drastic reduction in the optical pathlength compared to macroscale experiments. According to Beer-Lambert Law (Equation 2), the amount of light absorbed at a specific wavelength is directly proportional to the concentration ($c$) of the solution and to the optical pathlength ($l$) through the solution. This way, the reduced path length reduces the absorbance (A).

Thus, it complicates the effectiveness of the application of optical techniques in lab-on-a-chip (LOC) systems.

Several optofluidic techniques have been investigated to perform absorption spectroscopy by using microfluidic devices. The simplest technique is single pass absorption spectroscopy in which the signal absorbance is measured after its single pass through the sample. There is a trade-off between simplicity and poor limit of detection (LOD).

The literature contains an increasing number of reports which propose optical detection methods that mitigate the problem of short path length, including cavity-enhanced absorption spectroscopy (CEAS) [15, 16], and cavity ring-down spectroscopy (CRDS) [17, 18]. These optical detection methods have their own advantages and limitations in terms of simplicity, sensitivity and cost. The simplest technique of single-pass absorption spectroscopy based on a standard optical fiber geometry is usually limited to short interaction lengths (*in order of few mm*'s) due to the typical divergence of the beams coming from fibres or laser-written waveguides which limit the possible channel length because of the increased coupling losses [9].

The alternative technique to increase the optical pathlength is developing an optofluidic device with an optical channel in which the sample is placed within the channel or cavity comprising two highly reflecting mirrors. It is prudent to note that when employing CEAS, there are some difficulties in the alignment of optical fibres to ensure resonance. While these requirements enable efficient coupling of radiation into the cavity, it also introduces significant experimental complexity, which somewhat compromises the robustness of instruments for field applications. Furthermore, optical sensors based on integrated optical waveguides have been used to perform absorption spectroscopy [9]. Although, the use of waveguides has advantages, such as easy and precise alignment of the optical components with microfluidic channels [9], the relatively complex and costly process of waveguide fabrication limits their possibility to integrate on LOC. Each of these methods have their own limitations. The most important aspects that must be weighed against each other when choosing a spectrometric technique for a certain application are sensitivity, cost and complexity of the experimental setup.

Although there have been significant efforts to develop miniature devices to study chemicals and biochemicals, an interesting alternative approach we propose is to use a lensed fibre with collimated beam to achieve better sensitivity and low detection limit in comparison to a standard fibre.

## 2.2 Optical Fibres: Graded-index Fibres

Modern technology relies on high sensitivity sensors with capability to collect large amounts of data. To gather the data more efficiently and gain a competitive advantage, the sensors based on fibre optics are a promising possibility. Optical fibres have been used for numerous applications in telecommunications field and in biomedical field, such as long-distance data transmission and optical coherence tomography (OCT) [19]. The use of optical fibres to perform on-chip detection actually started in the early 2000s and ever since has gone through tremendous growth and advancement. The integration of fibres with microfluidic channels has proven a useful way to detect and control particles in samples [9, 18, 20, 21].

In this section, we introduce the principles of light transmission through the optical fibres, particularly focusing on graded-index fibre tips. Optical fibre is a cylindrical waveguide with the central glass (typically doped silica) called core, embedded by an insulated layer known as cladding. The structure of an optical fibre is illustrated in Fig.4. The coating layer and other upper layers encloses the cladding to protect the fibre from physical damage as shown in figure below.

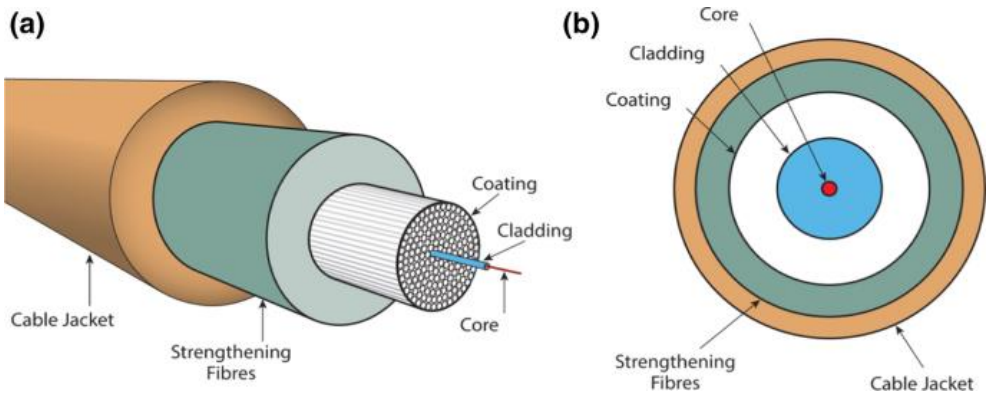


**Figure 4.** Structure of an optical fibre. Image adapted from [22].

The light propagates primarily along the fibre core where the light ray's incident on core-cladding boundaries, are totally reflected (total internal reflection) and are guided through the core without refraction as shown in the Figure 5 diagram.

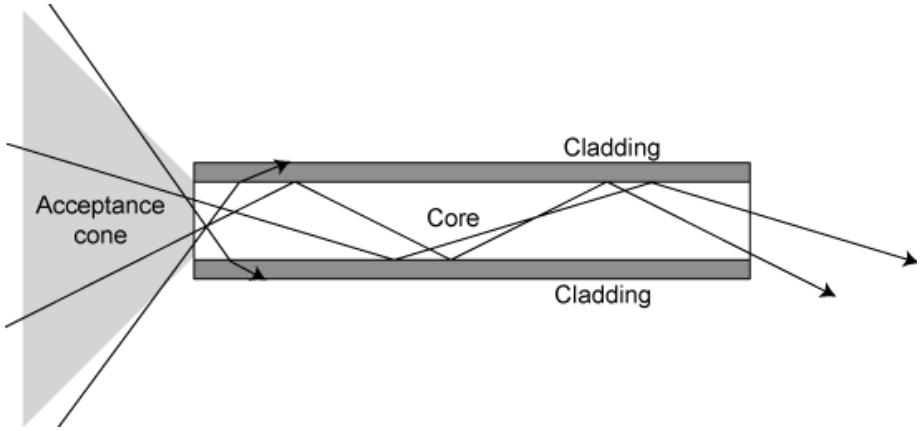


**Figure 5.** Propagation of light rays through an optical fibre. Image adapted from [23].

As mentioned above, optical fibres have been used in a wide range of applications and a variety of fibre structures have been developed according to the requirements of the application. Using optical fibres to perform detection on-chip is an excellent combination of two completely different fields, i.e., optics and microfluids, which merge to produce promising results. Optical fibres can easily be aligned with

microfluidic channels by etching U-groove or V-grooves on them, but micro-lenses need to be developed for implementation on compact and micro-scale devices.

Over the years, different fibre-lens have been developed according to the application and requirements of optofluidic devices. The micro-lensed fibres are the latest advancement of optical fibres in photonics field. Their radial symmetric refractive produces a variety of characteristics that are very valuable for the optofluidic field. They have the ability to control the beam size that propagates through the area/sample of interest. In this work, we used a micro-lens fibre called graded-index (GRIN) fibre or GIF tips. The GIF tips are lensed fibres which are fabricated by splicing the standard single-mode fibre (SMF) with coreless fibre (CF) and a then a segment of GRIN is fused to the end of CF, as shown in Figure 6. The GIF approach is directly analogous to free space coupling, in which the GRIN fiber lens is analogous to a bulk optical lens. The GIF based collimators have been demonstrated useful in various applications such as coupling light between optical fibres for transmission or collection purposes [24]. GIF tips have found significant use in recent years in optical coherence tomography (OCT) biomedical imaging and micro-electromechanical system (MEMs) applications but have only seen limited use outside of these fields [21, 24-26].

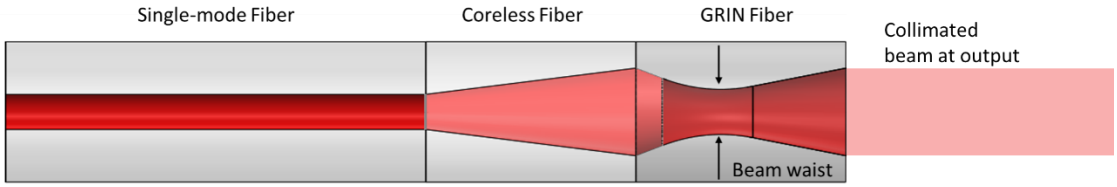


**Figure 6.** Schematic of GIF tip composed of a single-mode fibre spliced to a mode expanding coreless fibre, which is spliced to a graded-index fibre.

A coreless fibre is spliced between the SMF and GRIN fibres as shown in Fig. 6 to expand the beam coming out of SMF fibre. Therefore, the expanded beam is launched into GRIN fibre which either focuses or collimates the output beam depending on the GRIN fibre length. The figure below shows the light propagation comparison between two multi-mode fibres, the step index fibre and graded-index (GRIN) fibre. The GRIN fibres have a slowly varying refractive index along its radial axis which causes continues focusing and defocusing along the fibre length as shown in Figure 7, such that the output beam at GIF tip end can result in a collimated beam.

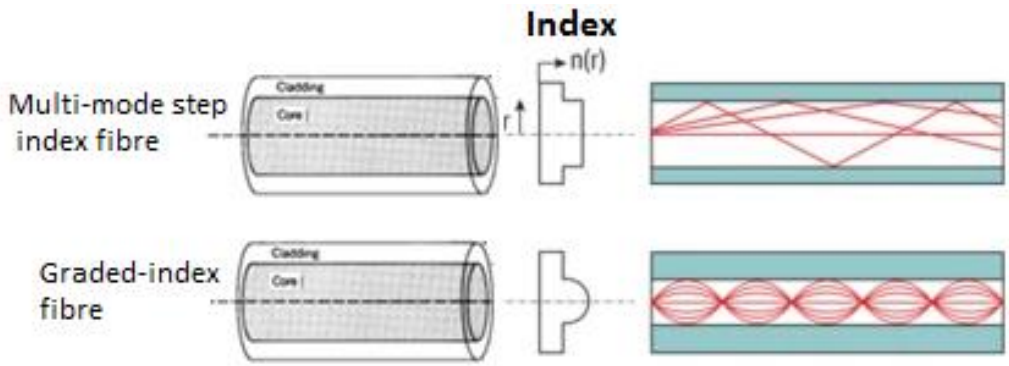


**Figure 7**. The ray trajectory and refractive index distribution of a multi-mode step index fibre and a multi-mode graded-index fibre with parabolic index distribution. Image adapted from [22].

The length of CF and GRIN fibre is estimated according to the desired spot size and collimated length of the beam, which will be discussed in the next chapter. One of the main purposes of using GIF tips in this work is to collimate the output light in order to have larger free space coupling lengths, which will not only reduce the beam divergence but will also decrease the optical losses. The light beam emerging from a typical single mode fibre (SMF) has a mode field diameter of about 10 μm [24], which outcomes as a highly divergent beam over the propagation distance. Due to the high divergence of beam, the optical losses are increased when light travels over a long distance. For this reason, the standard optical fibre's beam propagation is detectable only for a short distance.

## 2.3. Our Approach

This dissertation demonstrates laser absorption spectroscopy on a compact and miniaturized device using lensed graded-index (GRIN) fibre tips, which allow the development of a highly effective lab-on-a-chip platform. This chip scale platform is compact, fibre connectorized and does not require free-space optics to create the optical path.

We designed and fabricated an optofluidic device that makes significant inroads into increasing the interaction length for single pass absorption spectroscopy by using lensed graded-index fibre (GIF) tips. GIF tips enable the demonstration of a highly effective lab-on-a-chip absorption spectroscopy platform. The GIF tips have a collimated output that is transmitted longitudinally through a custom fabricated microchannel and is collected by a multimode fibre at the other end. In the next chapter, we demonstrate that this device can allow for absorption spectroscopy to be undertaken with sample volumes ten times smaller than standard cuvettes. This is particularly relevant for microvolume samples containing analytes such as proteins or antibodies. A proof-of-concept detection of a biologically relevant analyte, thiocyanate in artificial human saliva, is also presented.

Furthermore, we developed a new optofluidic device which has high feasibility for integration into lab-on-a-chip platform. The GIF tips are setup with interchangeable microchannels called pillar cuvette. The new cross-section configuration is developed to increase the optical pathlength for single pass absorption spectroscopy by maintaining the 2 µL – 3 µL of sample volume.

# Chapter 3

# Optofluidic Device Based on Graded-index Fibres

Considering the previous mentioned chapter, we developed an optofluidic device which makes significant inroads into increasing the interaction length for single-pass absorption spectroscopy by using lensed graded-index fibre (GIF) tips.

This chapter provides the rigorous details about the optofluidic device designs, and the fabrication process based on selected design. On the next stage to perform spectroscopic measurements with the device, the collection and excitation fibre (GIF tips) was designed according to the requirements. The basic concepts for designing GIF tips will be described in section 3.2. Furthermore, the experimental setup implementation will be explained to proceed with absorption spectroscopy measurements.

## 3.1. Device Design and Fabrication

The initial idea to design and develop the optofluidic device was based on a simple platform, that can hold and align the fibres. 8-channel V-grooves from *Precision Micro-optics* [27] were selected for fibre alignment. Based on this conceptual idea the optofluidic device was designed using the Solidworks software (version 2017) to get better combined overview of components. As shown in Fig. 8 the optofluidic device was fabricated using glass slides with high quality optical glass and precision v-grooves (sub-micron accuracy) for holding and aligning the fibre ends.

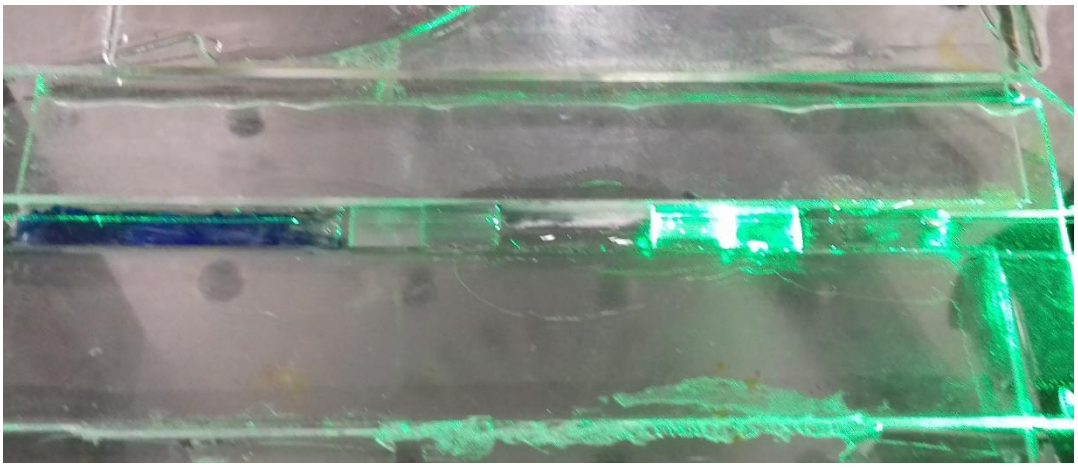

**Figure 8**. Optofluidic device based on glass slides.

These components were bonded together using NOA65 UV-curing adhesive to create a 200 µL - 300 µL microchannel as shown in close-up Solidworks design of Fig. 9b. To enhance single-pass absorption spectroscopy measurements within the microfluidic chip, the fabricated GIF tip (excitation fibre) was aligned to a Thorlabs M137L03 200 µm core multimode fibre (collection fibre) using the two spaced v-grooves (127 µm pitch). After precise insertion of the fibres into the v-grooves, the fibres were fixed using NOA65 UV-curable optical adhesive. The length of the channel between the excitation fibre and the collection fibre defines the optical path length which in this case was 10 mm.

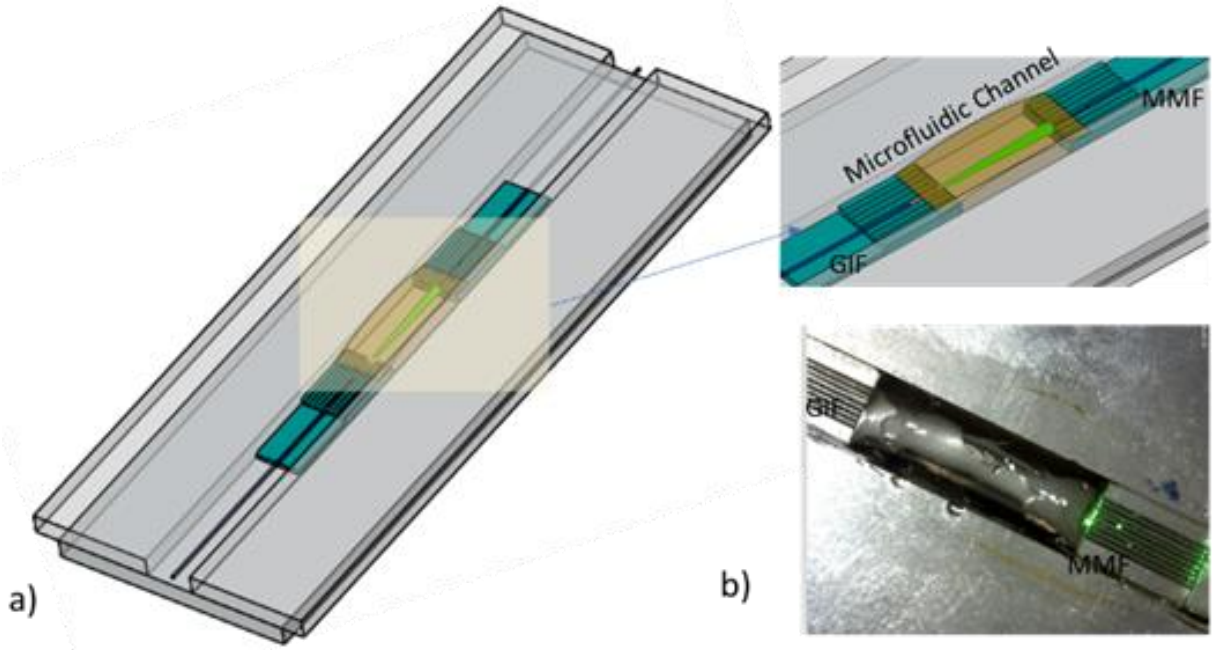


**Figure 9.** (a) Device Solidworks design showing microfluidic channel and GIF tip aligned to MMF within v-grooves (b). Close-up of microfluidic channel.

## 3.1.1. Integrated Optical Fibres

The GIF tips used in our experiments consist of three fibre sections spliced together as shown in Fig. 10. The incoming fibre is single-mode (SMF), followed by a section of coreless fibre (CF) that expands the beam, to transmit it to a section called GRIN as explained in the previous chapter. As GIFs have the same diameter as that of the SMF (~125 µm), they can be easily fusion spliced to a SMF with negligible loss.

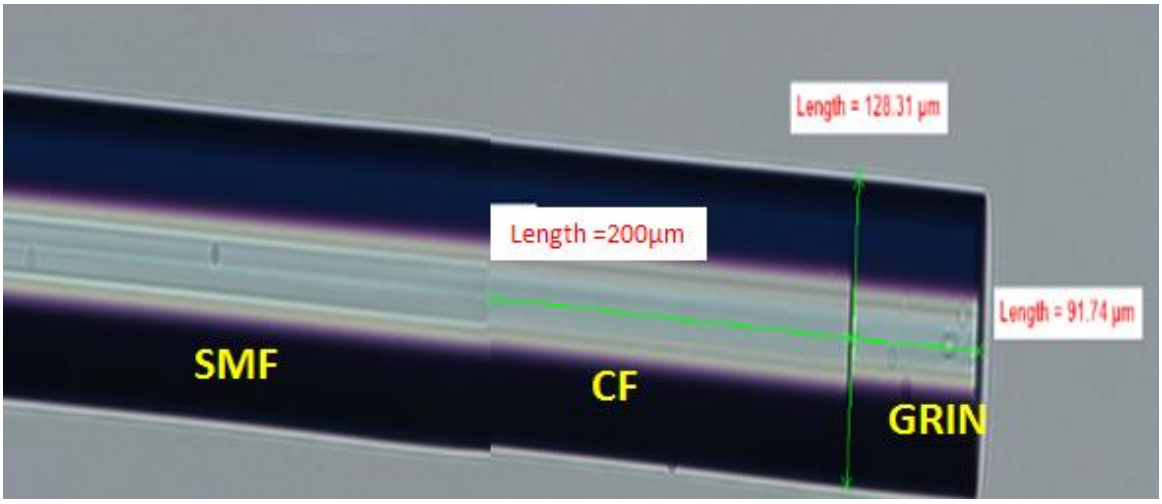


**Figure 10.** Microscope image of GIF tip with three spliced sections identified as SMF, CF and GRIN. The measured length of CF (200 µm) and GRIN (91.74 µm). The fibre diameter is 128µm.

In this work, we used Nufern GF1 single-mode fibre (NA = 0.13), Thorlabs FG125LA coreless fibre (CF) and Thorlabs GIF625 graded-index fibre (GRIN). As mentioned in section 2.1.2 the CF length and GRIN length are crucial parameters to determine the collimating or focusing performance of GIF tips. The RSOFT BeamProp software was used to perform simulations to estimate the length of GIF tip segments. For simulation purposes the refractive index data of standard single mode fibre (SMF) was adopted from [28] and coreless fibre (CF) is pure silica glass with refractive index $n=1.46$, as shown in the figure below.

The graded-index fibre tips have a parabolic refractive index profile that allows for a continual refocusing of the rays in the core and collimates the output beam. The GRIN fibre refractive index profile was measured through a IFA-100 refractive index profiler [29]. The below Figure 11 displays the refractive index profile of GIF, which shows that the maximum refractive index occurs at the centre of the fibre core, and gradually reduces along the radial axis.

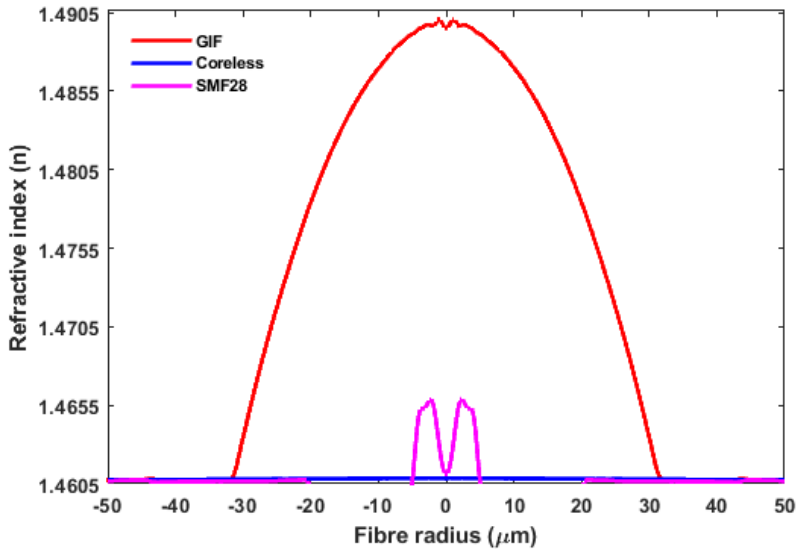


**Figure 11.** Refractive index profile of single-mode fibre (SMF28), coreless fibre and GRIN fibre measured at 532nm.

Appropriate segment lengths for minimizing the far-field divergence angle were derived (coreless segment ~ 200 µm, graded-index segment ~ 100 µm) using an optimization routine in which the coreless and graded-index fibre lengths were scanned over a large parameter space using RSOFT BeamProp/MOST. Figure 12 shows the contour plot of the far-field divergence angle (in degrees) as a function of coreless and graded-index segment lengths, that was used for optimizing the GIF tips at 532 nm. For this simulation the fundamental mode in the Nufern GF1 fibre was used. Slight variations in the beam divergence can be expected if higher-order modes are excited in the GF1 fibre. The beam divergence for the optimized GIF tip (1.31°) is much lower than for the SMF28 fibre (4.6°) at $\lambda = 532$ nm, which will be discussed in chapter 4. The GIF tips were fabricated by splicing 218 µm and 91 µm lengths of coreless and graded-index fibre segments, respectively, to the end of the GF1 SMF using a Fujikura fusion splicer (Tokyo, Japan). The fabrication process involves a precise thickness steel shims used in a straightforward process that we have developed around a standard commercial cleaver/splicer combination. In terms of repeatability, the fabrication tolerances for the lengths of the fibre segments were approximately ±10 microns, using the steel shims that achieve the required fibre lengths when splicing together the coreless and graded-index fibre sections to the single mode fibre.

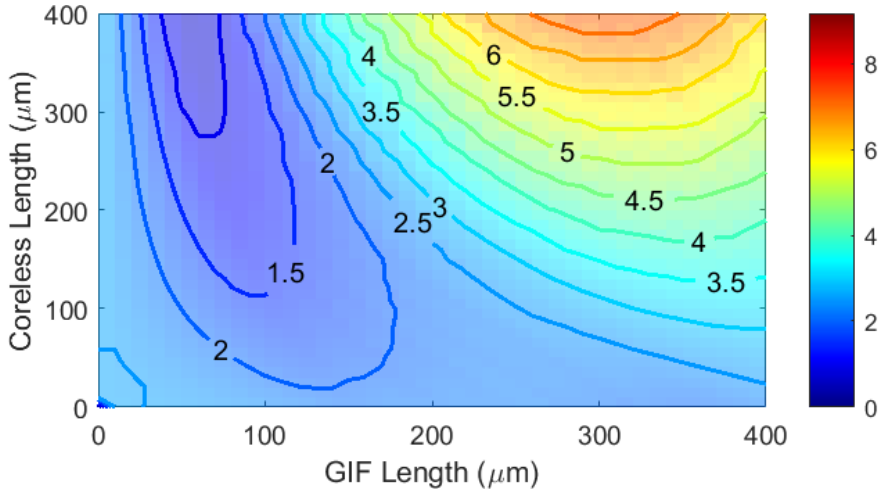


**Figure 12.** Contour plot of far-field divergence angle of GIF tips (in degrees) as a function of coreless and graded-index fibre segment lengths at λ = 532 nm.

At this point it is worth noting that whilst GF1 and SMF28 telecommunication fibres are classified and referred to as single-mode fibres, they are actually few-moded at visible wavelengths. This can have some minor influence on the beam divergence of both GIF tips and SMF fibres, although the launch conditions can be tweaked to ensure predominately fundamental mode excitation.

The GIF section acts as a collimating lens, whose purpose is to reduce the divergence angle of the exiting light beam, and thus increase the coupling distance range. It is expected that with this structure, the coupling efficiency between the excitation fibre (GIF) and collection fibre (MMF-multi mode fibre) would increase by a large extent. In the next chapter, the comparison between coupling losses of SMF-MMF coupling and GIF-MMF coupling will be presented and discussed.

### 3.1.2. Absorption Spectroscopy Experimental Setup

To measure absorption spectra, a broadband supercontinuum laser (YSL Photonics SC-OEM) was used as the excitation source and a Horiba iHR550 spectrometer was used as a detector. The supercontinuum laser (SC) emits light at wavelengths (λ) between 0.47 μm to 2.35 μm but only visible spectrum region ($0.47 \leq \lambda \geq 0.80$) was used due to the absorption features of the samples selected in this study. The spectrometer has spectral range between 200 nm and 1100 nm and the resolution is dependent on the grating spacing chosen for measurements.

To assess the performance of the optofluidics setup, the absorption measurements were also performed with a standard quartz cuvette (volume 3.5 mL) for comparison in a standard setup using the same input source as the microfluidic device and same detection system as shown in Fig. 13. Both setup configurations were designed and implemented to ensure the minimum changes and the experimental conditions for comparison. For this reason, both devices had the same interaction length of light with liquid, which is 10 mm. The

experimental setup is illustrated in Fig. 13 for the (a) standard cuvette and the (b) custom microfluidic device.

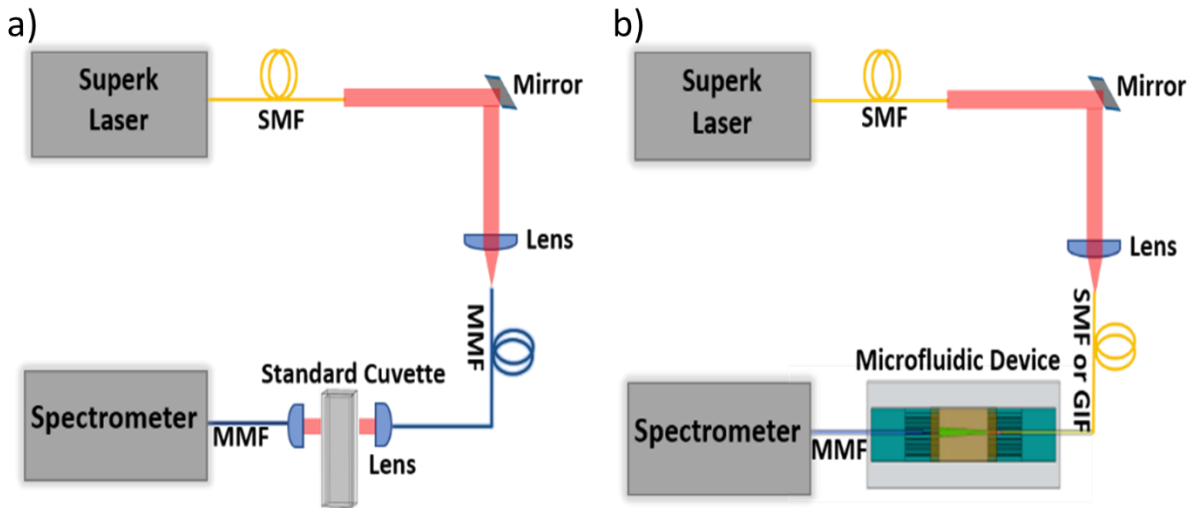


**Figure 13.** Experimental setup for absorption measurements with (a) standard cuvette and (b) microfluidic device.

A highly reflective mirror is positioned ~45º to reflect the collimated output beam of supercontinuum source. The reflected beam is focused into the excitation fibre, which is MMF for standard cuvette setup and SMF or GIF in case of the microfluidic device setup. For this reason, the setup used for microfluidic device is slightly different from the standard cuvette setup. In standard cuvette setup two lenses are used, one to collimate the output beam of excitation fibre and the other to focus the beam into the collection fibre. The lens system improves the coupling efficiency between the excitation and collection fibres, which means using a MMF fibre with high numerical aperture (NA = 0.22) doesn't affect coupling efficiency.

The excitation fibres used in microfluidic device setup are spliced to SMF28 with core size of 8 µm. The output collimated beam of supercontinuum laser is ~3 mm which means the selection of an appropriate lens is highly important, as shown in Fig. 14.

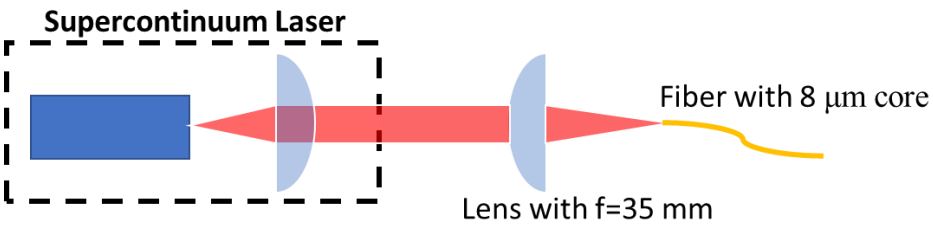


**Figure 14.** Schematic diagram of supercontinuum laser with internal lens and an external lens to focus the collimated beam.

The required lens' focal length (*f*) is calculated using the following equation:

$$2\omega_0 = \frac{4\lambda f}{\pi D} \qquad (3)$$

where $2\omega_0$ is the beam width at Rayleigh range and in this case, we require $2\omega_0 = 8\,\mu m$. $\lambda$ is the wavelength of interest, which is the visible region of the electromagnetic spectrum and D is the size of the collimated beam. The measured size of D at the output of the supercontinuum laser was ~3 mm and this way the calculated focal length $f$ of lens is approximately 35 mm, as shown in Fig 14. In order to obtain the highest efficiency at the output of SMF or GIF the lens and mirror properties (position, angle and height) were adjusted to maximize fluence at the focal region of the excitation fibre.

On the other hand, the standard cuvette setup required traditional optical lenses to collimate the output beam of the MMF (excitation fibre) and to focus the beam in the receiving MMF (collection fibre) as shown in Fig. 15. In the case of the microfluidic device, the collimated beam is directed longitudinally through the microchannel and collected by the multimode fibre (200 μm core size) at the other end (Fig. 9). The standard cuvette and GIF-enabled microfluidic chips were compared for a range of analytes including red food colour dye (Ponceau 4R Food Colour), thiocyanate (SCN) in water and thiocyanate in artificial human saliva, which are discussed in next chapter.

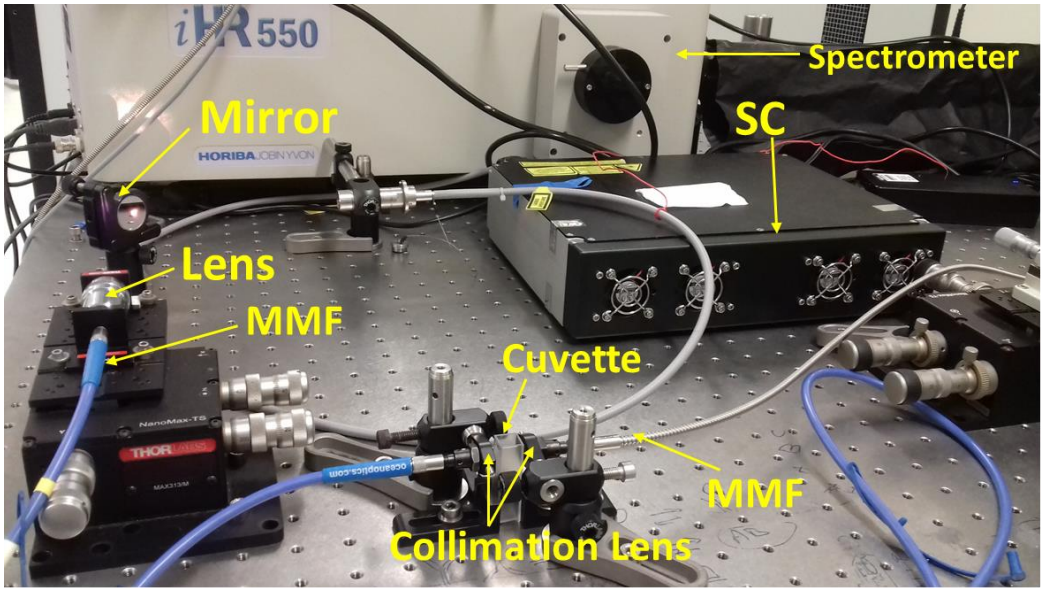


**Figure 15.** Photo of setup for standard cuvette measurements. SC: Supercontinuum Laser, MMF: Multi-mode fibre.

Fig. 16 presents the image of the devices used in this study for the a) standard cuvette filled with red food colour dye and b) optofluidic device with microchannel filled with red colour solution in which both excitation and collection fibre are immersed in the solution. The optofluidic device only requires 200 µL-300 µL of sample, but in our experiments a relatively large volume of solution is used to ensure that absorption does not vary because of evaporation of the aqueous solution throughout its experimental characterization. To avoid any cross-contamination between solutions of different concentrations, the optofluidic device is flushed with water between the measurements.

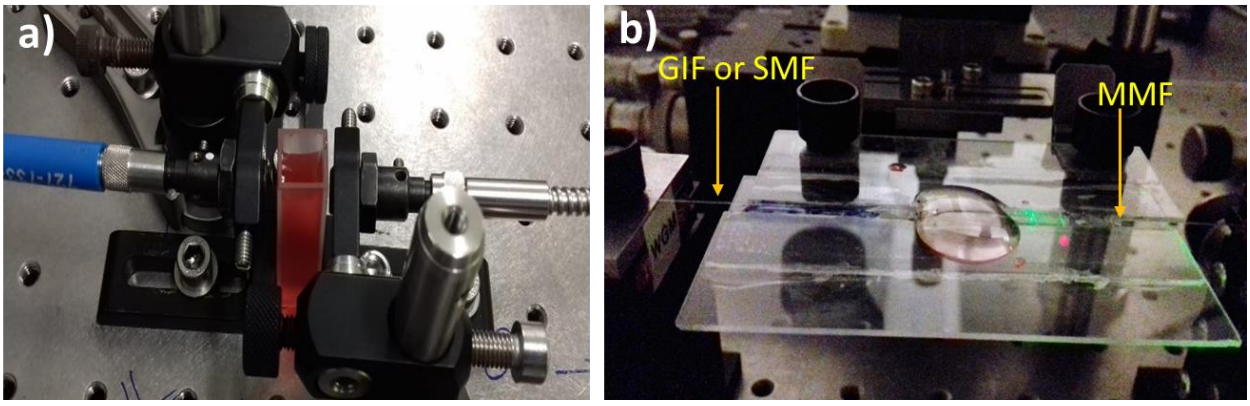


**Figure 16.** Image of device filled with red food colour dye sample for a) standard cuvette setup and b) optofluidic setup.

The measurements were performed using different concentration samples of red food colour dye, thiocyanate mixed in water and thiocyanate mixed with artificial saliva. In the next chapter, the absorbance data will be presented, which was calculated using the directly measured transmitted intensity of light through the sample of interest.

# Chapter 4

# Experimental Results and Discussion

This chapter will present the operational results obtained with the optofluidic device and standard cuvette using a simple solution of red colour dye. The GIF and SMF fibre divergence and propagation losses will be presented to justify the experimental conditions while using the fibres to collect the absorbance data.

Absorption spectroscopy is then demonstrated for iron (III) thiocyanate - $Fe(SCN)^{2+}$ prepared in water. Finally, the sensing platform is shown for the specific application of detecting the thiocyanate biomarker in artificial human saliva.

## 4.1. Red Colour Food Dye

The red colour dye (Pillar box red colour 50 mL, *Queen Est. 1897*) [30] was used to prepare the samples used in this study. The red colour dye initial solution of 200 mL was prepared by dissolving 2 mL of liquid food colour (124) in 180 mL ultrapure quality water with resistivity of $18.2\ M\Omega\ at\ 25°C$ (obtained with Milli $-$ Q® water purification system) [31] . The concentrations ranging from 5.45 µmol/L to 32.7 µmol/L were prepared diluting the initial solution.

Figure 17 shows the absorption spectrum of red food colour dye for concentrations ranging from 5.45 µmol/L to 32.7 µmol/L obtained with the standard cuvette setup. The absorbance is presented for wavelengths ranging from 400 nm to 600 nm using the supercontinuum source for all the range of concentrations. The spectral characteristics are collected by Horiba spectrometer with integration time of 1 s. As expected, and according to the Beer-Lambert law the shape of the absorbance spectrum shows less absorbance for diluted solutions (Fig. 17).

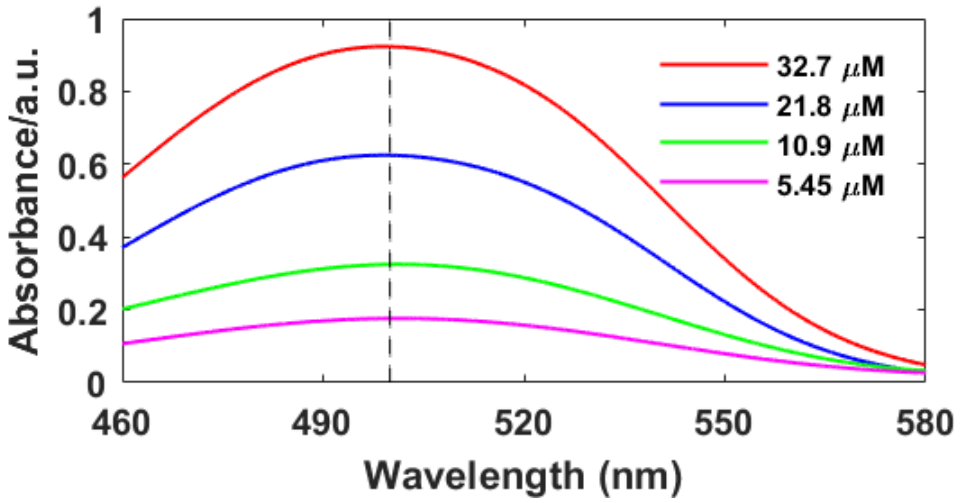


**Figure 17.** Relationship between absorbance and wavelength for red food colour concentration ranging from 5.45 µmol/L - 32.7 µmol/L. The absorbance spectrum obtained through spectrometer and using a standard cuvette with optical pathlength of 10 mm.

The absorption of the red food colour dye at its absorption peak of 501 nm (Fig. 17) as a function of dye concentration (5 µM to 33 µM) for both the standard cuvette and the custom GIF-enabled microfluidic chip is shown in Fig. 18. To mitigate the effect of laser instability during the experiments, the transmitted power *I* for each measurement is normalized to the power recorded ($I_o$) each time prior to filling the microchannel with different concentrations of analyte. The absorbance measurements at each concentration, *A*, were obtained by taking the ratio of the normalized transmitted power *I* to the power $I_o$ recorded in absence of the analyte of interest according to the Beer-Lambert Eq (2).

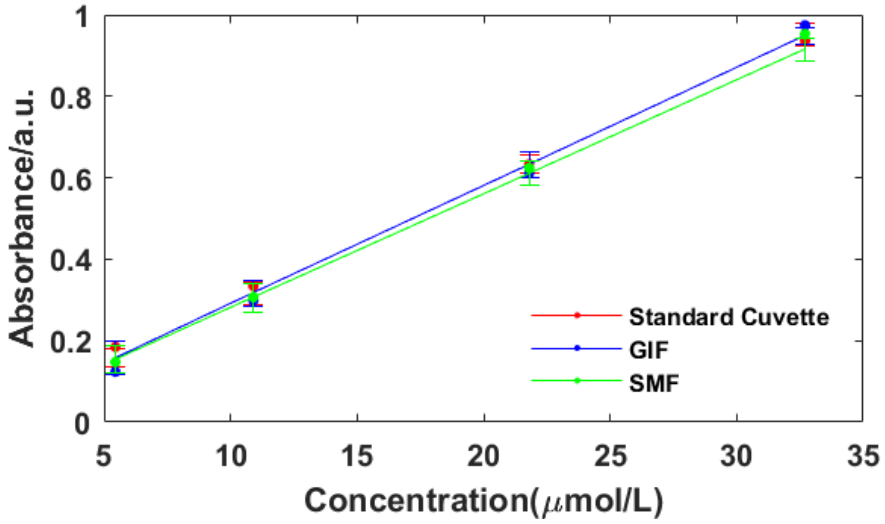


**Figure 18.** Plot of absorbance at $\lambda_{max} = 501\ nm$ of red color dye for a standard cuvette and the optofluidics chip with either GIF tip or SMF fibre, where the linear regression is A = 0.029*c according to Eq. (2).

The calibration curves in Fig. 18 clearly show the linearity of absorbance with dye concentration, according to the Beer-Lambert law, Eq. 2. The molar absorptivity can be determined by the slope of the linear regression plotted in Fig 18. The molar absorptivity value is $\varepsilon \approx 28{,}891\ L.mol^{-1}cm^{-1}$, which is in agreement with the literature ($\varepsilon \approx 30{,}000\ L.mol^{-1}cm^{-1}\ at\ \lambda_{max} = 505\ nm$) [32]. The quantitative analysis shows the ability to reproduce linearity using a microfluidic device with only ~200 µL of solution compared with the 3.5 mL standard cuvette, while maintaining the same interaction length. This is particularly noteworthy given that only small sample volumes are commonly accessible in point-of-care diagnostics.

## 4.2. Fibre characterization

Although the optofluidic device absorbance results are comparable when using the standard SMF28 fibre and the GIF tip, the significantly higher beam divergence of SMF means there is lower collection efficiency at the MMF. For this reason, higher power is required in the SMF (120 µW at output of fibre) compared to the GIF tip (70 µW at output of fibre) to achieve similar signal-to-noise ratios (SNR) in spectroscopic measurements performed in this study, as illustrated in the diagram of Fig. 19. Since GIF has proved its potential in absorption spectroscopy measurements, particular interest has been placed on accurately characterizing its parameters, especially the beam divergence and coupling losses between the excitation and collection fibre.

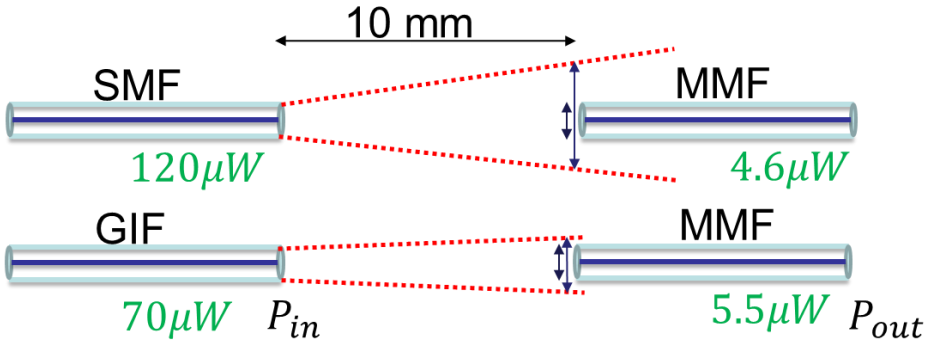


**Figure 19.** Illustration diagram of output power at the MMF according to the power at the end of SMF and GIF.

In this section, we study the beam divergence of both fibres and analyse the coupling losses between the excitation and collection fibre for both SMF and GIF configuration presented in above experimental setup for optofluidic device. In photonics applications, the information about beam size and its intensity profile at a given distance are important parameters to study the performance of an optical fibre. In fibre optics, it is generally acceptable to treat the output light as a Gaussian beam and this approximation is used to predict the divergence of the output beam of an optical component. The output beam from a cleaved optical fibre

is considered as having a cross-sectional intensity distribution of a Gaussian profile [33]. The beam radius ($\omega$) of the Gaussian beam varies along the propagation direction (z) and can be approximated as:

$$\omega(z) = \omega_o \sqrt{1 + \left(\frac{z\lambda M^2}{\pi {\omega_o}^2 n}\right)^2} \qquad (4)$$

where $\omega_o$ is the beam radius at z = 0, which is also called beam waist. The beam size (diameter/radius) is minimum at the beam waist and it increases along the propagation distance according to Eq. (4). Here *n* is the refractive index of the beam propagation medium, in this case n =1 (air). $M^2$ is the beam quality factor (represents the degree of variation of a beam from an ideal Gaussian beam) and z is the propagation distance form the end face of the fibre.

The beam divergence characteristics of the GIF were measured and compared against SMF28 fibre used in spectroscopic experiments. In this experiment the beam divergence of the GIF and SMF were measured using an Ophir Spiricon silicon-based CCD camera (beam analyser). The experimental setup used to perform these measurements is illustrated in Fig. 20. The GIF/SMF fibre was placed on a 3-axis stage which moves in z direction to increase the distance between fibre end face and beam analyser. Therefore, it measures the beam width at distance z.

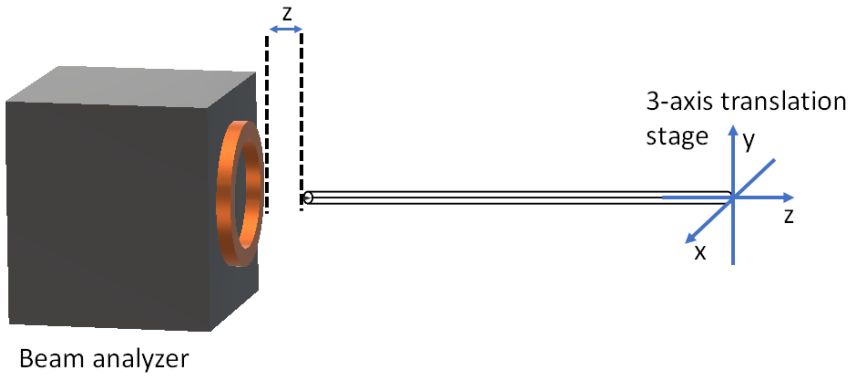


**Figure 20.** Schematic representation of the beam profile measurement setup. The fibre was positioned by a 3-axis translation stage and aligned with the input aperture of the Spiricon CCD Camera detector.

The image in Fig. 21 represents a 2D display of the beam profile in which colour represent the power intensity, i.e., high-power intensity at the centre of beam. Since the Gaussian beam has no sharp edges, the radius or diameter of the beam is defined as the distance from the beam axis to the distance where beam intensity drops to $1/e^2$, which is nearly 13.5% value of beam intensity at beam axis. The below image clearly shows that SMF has highly divergent beam compared to GIF output beam, at same distance from their respective ends.

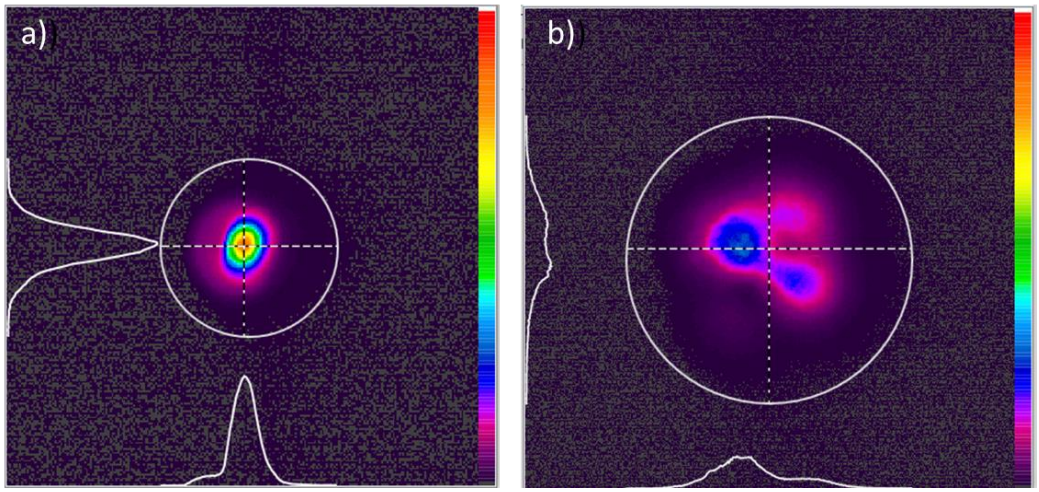


**Figure 21.** The 2D beam profile of a) GIF with coreless segment ~ 200 µm and GRIN segment ~ 100 µm; b) SMF modal nature. The beam profile is measured with Spiricon CCD camera at 0.8 mm distance from the end-face of fibre.

The beam radius data collected along the distance (z) is plotted in the graph of Fig. 22. It compares the diverging beam radius of the SMF and the GIF tip as a function of propagation distance at wavelengths of 532 nm and 650 nm, respectively. As predicted, the beam divergence is relatively insensitive to wavelength changes of the order of ~100 nm.

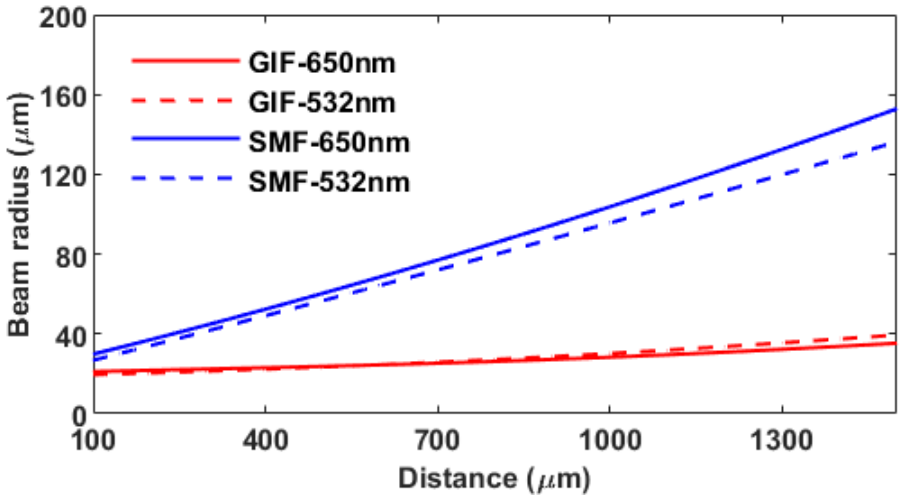


**Figure 22.** Measured beam radius of SMF28 (blue curves) and GIF tip (red curves) as a function of propagation distance at 532 nm and 650 nm.

The far-field divergence angle of both fibres is shown in Fig. 23, in which transverse dimension of the beam is plotted over the propagation distance. The beam divergence for both fibres is calculated by using the tangent trigonometry function between the beam radius and distance. The GIF tip presents a near-collimated

beam of 1.3º far-field divergence angle, which is approximately 4× lower than the 4.5º far-field divergence angle for SMF28 fibre at 532 nm.

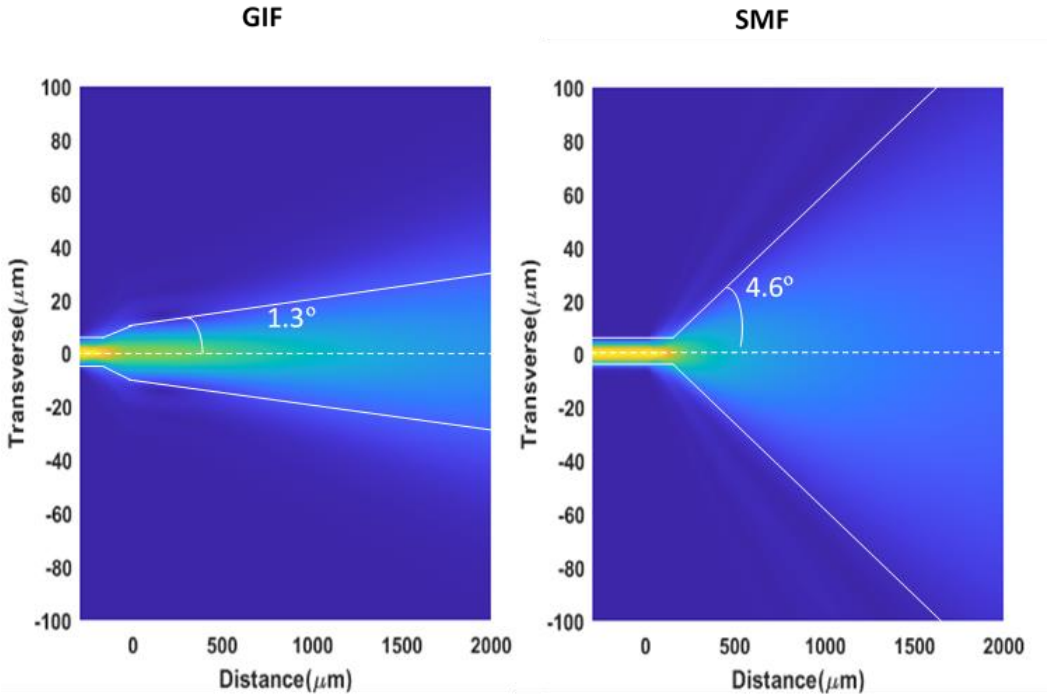


**Figure 23.** The beam divergence of SMF28 and the GIF fibre (CF = 218 μm and GRIN = 91 μm) as a function of their beam propagation. The values are calculated using the data plotted in Fig. 22.

Furthermore, to characterize the fibre's performance in absorption spectroscopy, the insertion losses ($I_L$) between the excitation and collection fibre has been studied. The insertion losses are related to the coupling efficiency between fibres and by divergent beam propagation, which is responsible for transmission loss.

To study the coupling and transmission losses between SMF-MMF and GIF-MMF fibres as a function of channel length, an optical power meter (Thorlabs S120C, PM100D) was used to measure the output power of the MMF. The experimental setup used in these measurements is illustrated in Fig. 24, in which JDS Uniphase single wavelength CW laser beam operating at $532\ nm$ is focused into GIF or SMF fibre to measure the optical losses at the output of MMF.

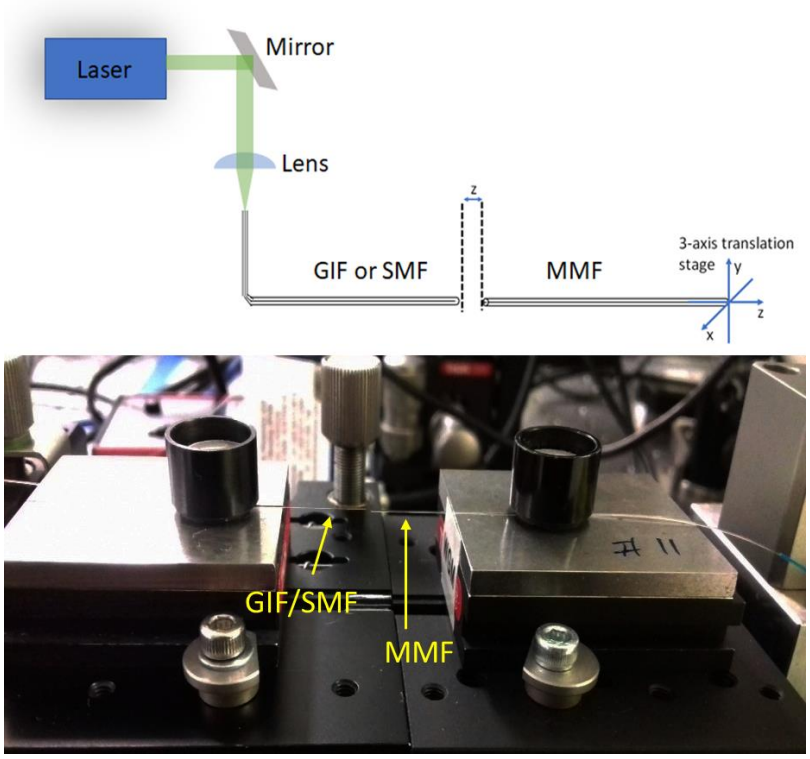


**Figure 24.** Schematic representation of the insertion loss measurement setup. The MMF fibre was positioned on a 3-axis translation stage and aligned with the excitation fibre (GIF/SMF). The MMF fibre is moved in z axis over the 10 mm distance from end-face of excitation fibre.

The comparison of the insertion losses between SMF-MMF and GIF-MMF is shown in Fig. 25. For a fixed distance between excitation and collection fibre the insertion losses are calculated by the ratio between power at end of MMF and power measured at end of SMF or GIF, as expressed in Eq. (5). Each data point shown in Fig. 25 was generated by averaging over 10 scanning events.

$$I_L = -10log_{10}\left(\frac{P_{out-MMF}}{P_{out-SMF/GIF}}\right) \qquad (5)$$

where $P_{out-MMF}$ is the output power of MMF fibre, $P_{out-SMF/GIF}$ is the power at the end of SMF or GIF tip fibre and $I_L$ is the insertion loss.

The comparison of SMF-MMF and GIF-MMF insertion losses is shown in Fig. 25. The gap size of 10 mm between fibres delivers the best results with GIF fibre keeping the losses relatively constant and lower than 4 dB. Therefore, in SMF setup the coupling length variation of 10 mm increase the losses by nearly 16 dB. The graph shows that for a fixed distance between the excitation and collection fibres (10.0 mm), the insertion optical losses can be 15× lower when using the GIF tip fibre.. In addition, the GIF setup has 4×

less optical losses compared to waveguide integrated optofluidic devices presented by for example Malic et al. [9].

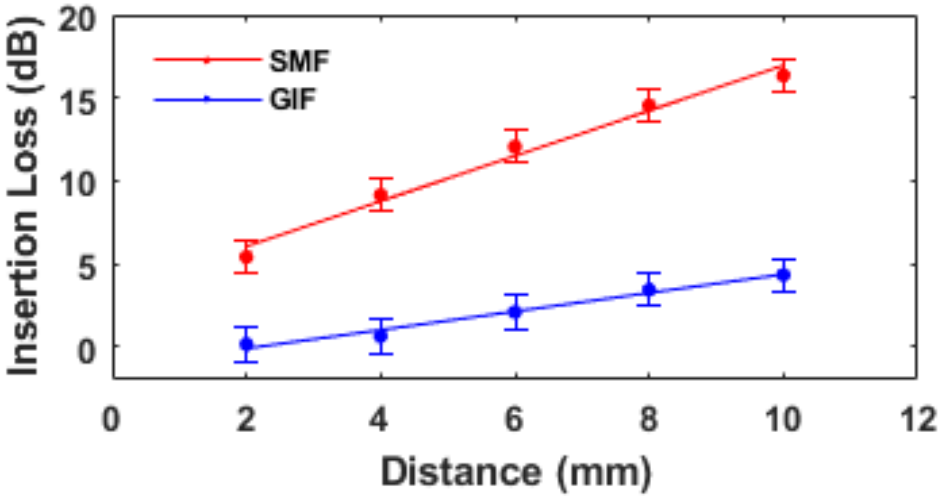


**Figure 25.** Measured insertion losses of GIF-MMF and SMF-MMF configurations.

In comparison, the insertion losses shown for GIF setup in Fig.19 are slightly different from results in Fig. 25. The insertion losses presented in Fig. 19 for GIF setup is 11 dB, which is 2× higher compared to same distance in Fig.25 for same setup. The discrepancy in both values is due to the adjustments required for input and output power while performing the experiments with samples. The $P_{in}$ (Fig.19) value was drastically decreased to avoid the thermal instability on optofluidic device.

This effectively means the GIF setup could be used for significantly longer channels for a given permissible insertion loss. The low coupling losses in microfluidics allow for low power to be used which avoids potential issues such as bleaching of the sample if higher powers were required. This shows the significant benefits of using GIF tips in fibre connectorized lab-on-a-chip spectroscopic applications.

## 4.3. Iron (III) Thiocyanate $[\mathbf{Fe(SCN)^{2+}}]$ in Water

To further demonstrate this optofluidic device, we show that it can be used for detection of biologically relevant analytes such as thiocyanate. Thiocyanate was chosen as it is of interest in medical diagnostics [34], because it is a detoxification product of cancer treatments and an indicator of oral health including exposure to passive smoking [35] which can significantly increase thiocyanate concentrations to levels potentially capable of affecting the thyroid gland. Salivary thiocyanate concentration in non-smokers ranges from 0.5 to 2 mM whereas smokers may have salivary concentration ranges from 2 to 6 mM [36].

The complexation reaction between the Fe (III) ions and SCN ligands (non-metal) forms a red-orange colour compound, iron (III) thiocyanate $[Fe(SCN)]^{2+}$, which allows for colour techniques such as absorption spectroscopy to be used for its detection.

$$Fe^{3+} + SCN^{-} \rightleftharpoons Fe(SCN)^{2+} \qquad (6)$$

The iron (III) thiocyanate solution was prepared by mixing separately a prepared iron solution in nitric acid and thiocyanate solution in Milli-Q water. The initial thiocyanate solution is diluted as required, to make standard solutions over the range of concentrations used in this study. In order to perform a complete analysis of absorption by thiocyanate (SCN), a solution of ($Fe^{3+}$) and water was used as the reference. Absorption measurements at 480 nm (peak absorbance of $[Fe(SCN)]^{2+}$) were performed using the same setup as before, mixing in 1:1 ratio by volume various thiocyanate concentrations (50 µM to 410 µM) with a 26.4 mM concentration of Fe (III). Note that after mixing the thiocyanate solution with the Fe (III) solution, fading of the colour over time occurs [37]. Some studies have suggested that the fading is due to thiocyanate ion reduction of $Fe^{3+} \rightarrow Fe^{2+}$, but the goal of our measurements is not to examine the cause of fading. To avoid this, the absorbance measurements were performed immediately after mixing the two reagents.

Fig. 26 display the absorbance spectrum of complex iron (III) thiocyanate for the different concentration of thiocyanate. It is possible to observe from spectrum that at higher wavelengths (480 nm -540 nm) the decay reaction is faster in comparison to low concentrations of thiocyanate and this is consistent with the trends observed in the literature [37].

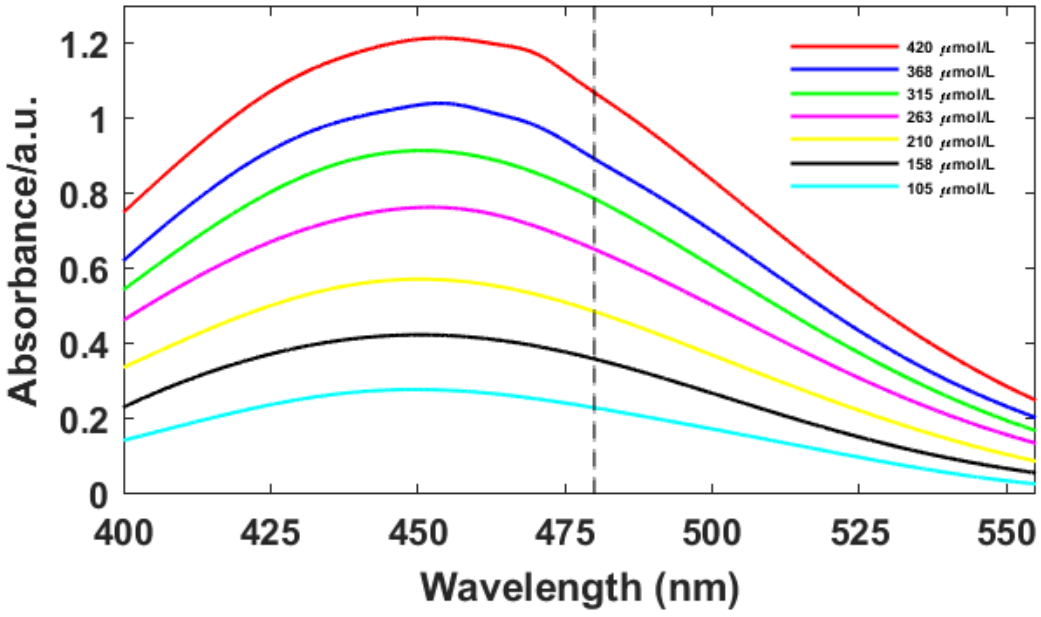


**Figure 26.** Relationship between absorbance and wavelength for $Fe(SCN)^{2+}$concentration ranging from 105 µmol/L - 420 µmol/L. The absorbance spectrum obtained through spectrometer and using a standard cuvette with optical pathlength of 10 mm.

Figure 27 shows the absorbance as a function of the SCN concentration for the three configurations described, with the results showing comparable linearity according to the Beer-Lambert Law. Based on the Beer-lambert law the molar absorptivity of $Fe(SCN)^{2+}$ at the wavelength of 480 nm can be determined as, $\varepsilon \approx 2389\ L.mol^{-1}cm^{-1}$ which is the slope of linear fit since the optical pathlength is 1 cm in this case. This is lower than the reported value in the literature (i.e., λ = 480 nm, ε = 3914 $L.mol^{-1}cm^{-1}$ ; λ= 500 nm, ε = 2900 $L.mol^{-1}cm^{-1}$ with ionic strength being 0.5) [38], most likely due to the lower ionic strength in our solutions (i.e., 0.1) compared to that used in the literature.

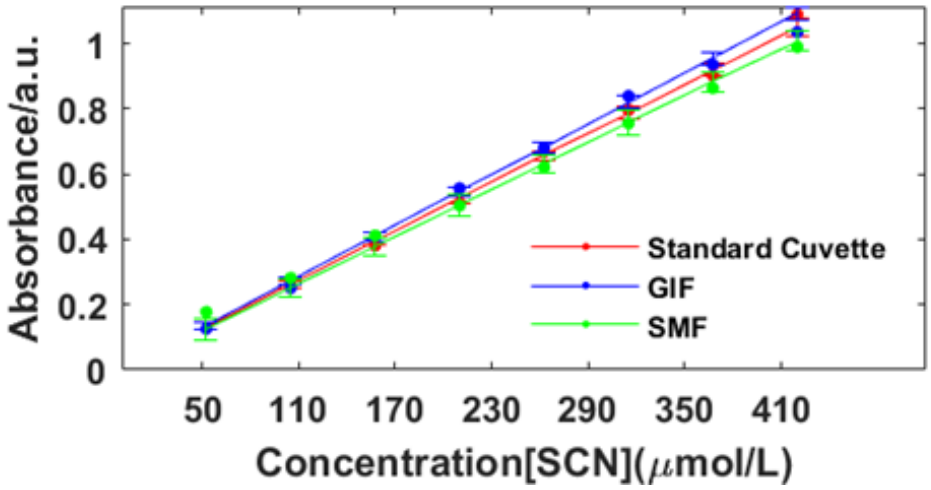


**Figure 27.** Plot of absorbance at 480 nm for $Fe(SCN)^{2+}$solution as a function of $SCN^{-}$ concentration in water for standard cuvette (A = 0.0025C) and for the microfluidic chip with either GIF (A = 0.0026C) or SMF (A = 0.0024C).

The uncertainty in the measurements was determined from the standard deviation of 10 measurements taken of the spectrum over a duration of 100 seconds. The uncertainty in value of absorbance is calculated using the following equation:

$$\Delta A = \frac{\Delta I_o}{I_o} + \frac{\Delta I}{I} \qquad (7)$$

where $\Delta I_o$ and $\Delta I$ are the uncertainty in 10 measurements of $I_o$ and $I$, respectively.

## 4.4. Iron Thiocyanate $[\mathbf{Fe(SCN)^{2+}}]$ in Artificial Saliva

We also explored the GIF tip enabled optofluidic setup for thiocyanate detection in a more complicated sample matrix other than water, artificial saliva, underpinning its potential for point-of-care diagnosis. The results were therefore repeated by preparing the $Fe(SCN)^{2+}$ solution in artificial saliva.

The artificial human saliva was synthesized by composition of the SAGF medium [39]. This involved mixing sodium chloride (125.6 mg), potassium chloride (963.9 mg), calcium chloride (227.8 mg), potassium phosphate monobasic (654.5 mg), urea (200 mg), sodium bicarbonate (630.8 mg), disodium sulfate decahydrate (763.2 mg) and ammonium chloride (178 mg) in 1 L of Milli-Q water. Different amounts of sodium thiocyanate were added into the solution to prepare a series of thiocyanate solutions.

The results in Fig. 28 show the linearity and comparable absorbance at 480 nm for the SCN in water and artificial saliva. This successful demonstration shows that it is possible to extend the tests of these optofluidic chips to saliva, which is a typical biological sample. In present study, the lowest detected value of SCN concentration was 50 µmoL/L which is much lower when compared to required values to distinguish smokers and non-smoker [40]. This proves the high sensitivity of device and its relevance to use for medical applications.

The limit of detection (LOD) of this simple but practical optofluidic device is defined as the minimum reliably detectable concentration of SCN and it can be determined using the following equation:

$$LOD = \frac{3\times\sigma}{s} \qquad (8)$$

where s is the slope of the calibration curve and $\sigma$ is the standard deviation of the lowest concentration measured and it can in this case, be determined as 16.2 µM. Salivary thiocyanate could for instance be used to evaluate the influence of passive smoking on public health or e.g., detect thyroid gland malfunction.

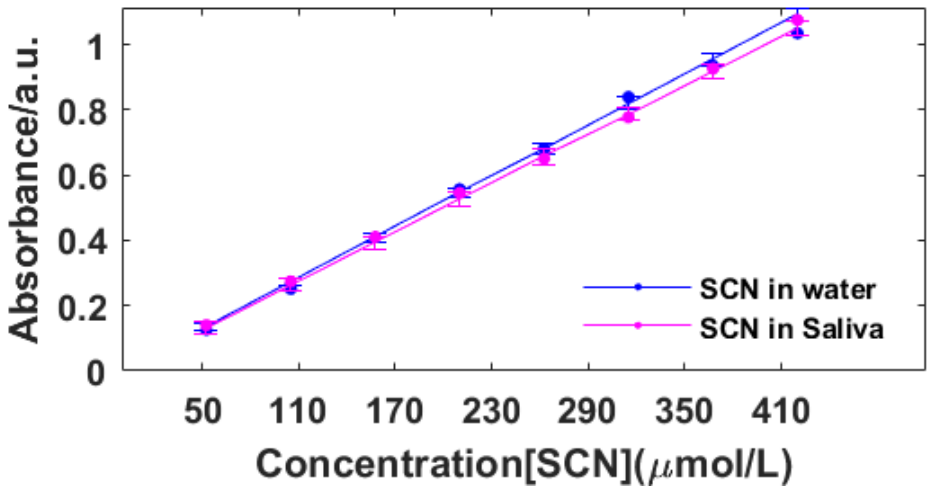


**Figure 28.** Plot of absorbance at 480 nm as a function of SCN solution in artificial saliva (A = 0.0025C) and in water (A = 0.0026C) for the GIF setup.

Although other techniques exist to detect thiocyanate such as surface-enhanced Raman spectroscopy using droplet microfluidic chips [41], and chromatography mass spectroscopy [42], we present a simple and compact fibre-coupled platform to achieve detection, with the technique presented being extendable to cavity-enhanced approaches which would further enhance sensitivity.

# Chapter 5

# Pillar Cuvette

The demand for simple and inexpensive microfluidic chips integrated with optics is growing in analytical sciences. Recent research has been devoted to the development of miniaturized and compact devices with the goal of integrating them into a lab-on-a-chip platform.

In the previous chapters of this thesis, we demonstrated the ability of GIF tips to integrate on an optofluidic device and their advantages over the SMF. The developed optofluidic device was a compact device and GIF tips was easily integrated on it. However, the device doesn't have compatibility to be integrated on lab-on-a-chip platform due to the difficulty of sample/liquid changing between the measurements. To avoid the contamination between the measurements the microchannel had to be rinsed with water. For this reason, we proceed to develop an optofluidic device with a sample holding chip (Pillar cuvette) which had been used in previous work by Priest *et al.* [43, 44].

In this study, we used a quartz glass microfluidic chip with a micropillar array (i.e. pillar cuvette), designed and fabricated at the University of South Australia. The term "pillar cuvette" refers to a cuvette embedded with micro pillars to hold the liquid samples for their analysis. The pillar cuvettes are compact and interchangeable devices which requires only ~2 µL sample volume to perform any form of optical spectroscopy including reflectivity, fluorescence, transmission and absorbance spectroscopy [43]. Our research particularly focuses on using pillar cuvettes for absorption spectroscopy with integrated optical components. Fig. 29 illustrates the design of a pillar cuvette chip in 3D. The pillars are in an ordered array in which the dimensions of pillars and interpillar spacing are uniform. The liquid inserted in the loading area/reservoir flows through the hydrophilic micro-scale pillars i.e. wicking of liquid in a square array of pillars [44] as shown in Fig. 29.

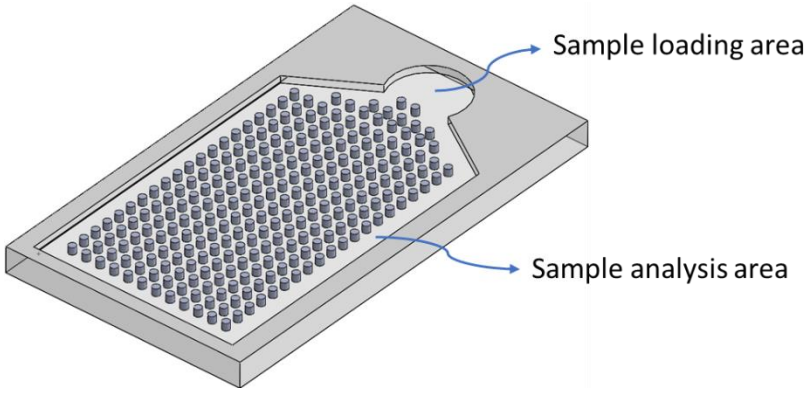


**Figure 29.** 3D schematic design of a pillar cuvette with sample loading area and analysis area covered with micro-scale pillars, fabricated at University of South Australia. Note that the pillar size and the device size is not to scale.

The use of the pillar cuvette will have a number of advantages to perform spectroscopic analysis, compared to a conventional optofluidic device reported in the literature. The spectroscopic analysis can be performed

with high concentrations which will bring the relief from dilution method. Also, the clinical samples with low concentration are possible to detect which will be demonstrated in coming sections.

## 5.1. Pillar Cuvette Fabrication

Pillar cuvettes are fabricated using the UV-photolithography technique and plasma etching of a substrate [45] e.g. quartz glass or fused silica. UV-photolithography is the most widely used lithography technique in the fabrication of nano or micro scale structures. It is developing field with $200 billion industry worldwide [46], which provides a path to bring nanoscale devices from the lab to everyday life. The pillar cuvette chip fabrication steps are shown in diagram of Fig. 30.

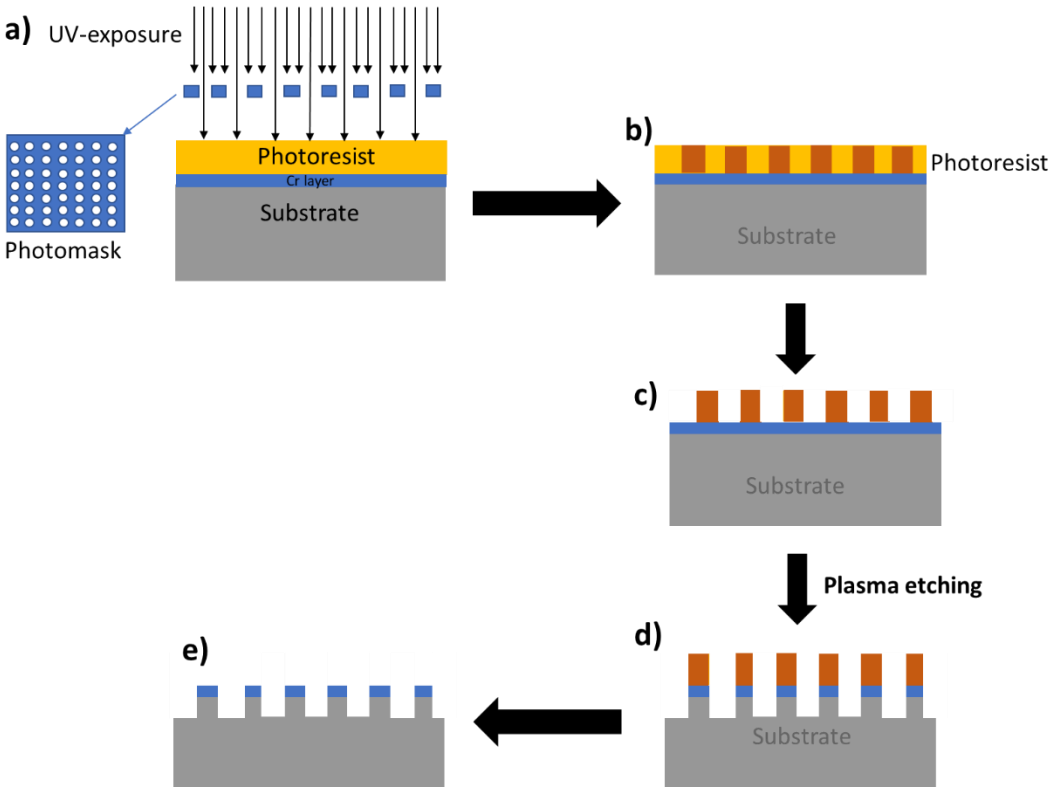


**Figure 30.** Schematic diagram of micropillar fabrication by UV-lithography. a) UV-exposure of substrate coated with thin chromium layer and spin-coated photoresist, through a photomask. b) The UV-exposed area changes in chemical properties of photoresist. c) Unwanted photoresist (unexposed areas) is removed by washing it with Piranha solution. d) Plasma etching of chromium layer.

To fabricate pillar cuvettes a quartz glass or fused silica substrate is coated with a thin layer of chromium (Cr) to ensure the adhesion of photoresist with substrate. The photoresist material is deposited over the substrate by spin-coating, forming a thin and uniform film. The coated sample is exposed to UV radiation

through a photomask as shown in Fig. 30a, which transfers the pattern of photomask to coated substrate. The exposed areas of photoresist material undergo changes in chemical properties (Fig. 30b) and then the substrate is dissolved in a developer solution to remove the unexposed area of photoresist and to replicate the substrate with the pattern of photomask (Fig. 30c). After the essential process, the plasma (C3F8) is generated to proceed with plasma etching of Cr thin layer and then sample is washed with Piranha solution at room temperature (Fig. 30d).

The pillar cuvettes used in this study have pillars which are cylindrical, but they can be made in different shapes and sizes and formed in an array with large number of elements. This fabrication technique demonstrates that it is possible to custom design the pillar height, width and nanopillar density as shown in Fig. 31. This structure and array of pillars forms multidirectional 3D fluidic channels to flow the liquid in thin film shape. These chips have shown improved efficiency compared to planar flow in terms of particle separation.

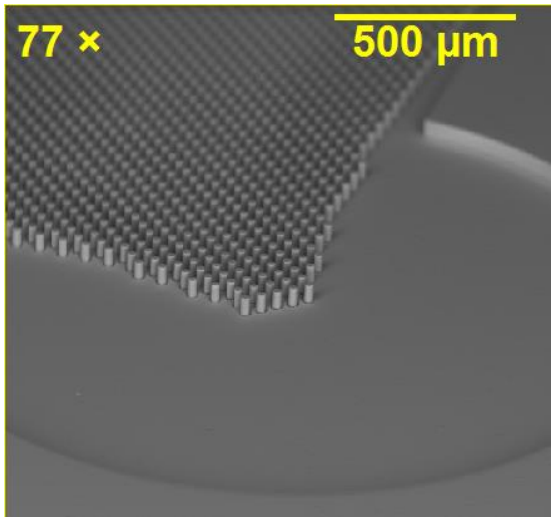


**Figure 31.** Scanning electron microscope (SEM) image of micropillars with side view.

## 5.2. Absorption Spectroscopy Using the Pillar Cuvette

As mentioned above the pillar cuvette chip can be used to perform absorption spectroscopy and was used in previous work performed by Priest *et. al.* Reference [43] shows the absorption spectroscopy measurements with micro-scale pillars. A detailed description of pillar cuvette, spectroscopic measurements setup and data analysis method are described in journal articles [43, 44].

Fig. 32 illustrates the setup used in the previous study to perform the absorption spectroscopy. The pillar cuvette chip is illuminated from bottom and the light with changed properties is collected by placing a detector on top of pillar cuvette as shown in the below image.

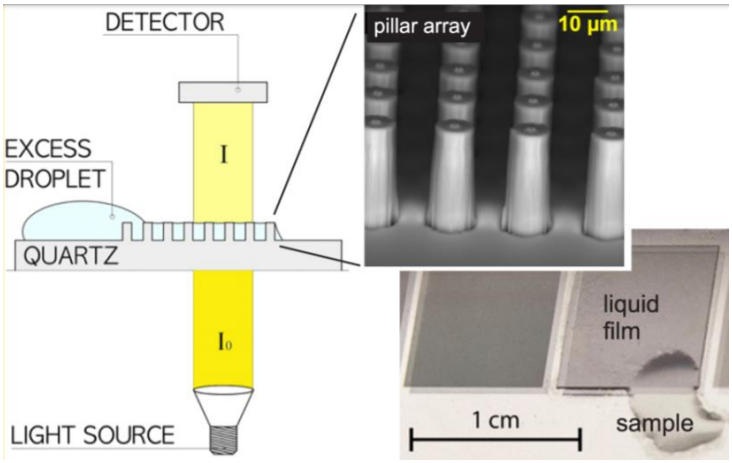


**Figure 32.** Schematic of experimental setup used to perform absorption spectroscopy with Pillar cuvette using transverse section. The image shows the side view of pillars whose base is illuminated by the light source. Image adapted from [43].

In this configuration, the pillar cuvette represents an effective single-pass absorption spectroscopy platform with only ~2 µL of sample volume needed and with optical pathlength *l* which is defined by the pillar height (thus, the liquid film thickness). The optical path length is limited to 10-50 µm which is 200× smaller than commercially available standard cuvettes (10 mm) used in spectroscopic measurements.

In the medical field, interest grows in understanding proteins to help determine the molecular basis of diseases associated with them. In addition, new techniques are developing to detect sufficiently low quantities of proteins, which would lead to the ultimate in early detection of diseases. Proteins are extremely important molecules composed of amino acids, which are organic compounds and amino acids are the building blocks of proteins. Amino acids contain aromatic side chains i.e. tyrosine and tryptophan [47], which are responsible for absorbing UV-light at a wavelength of 280 nm as shown in Fig. 33.

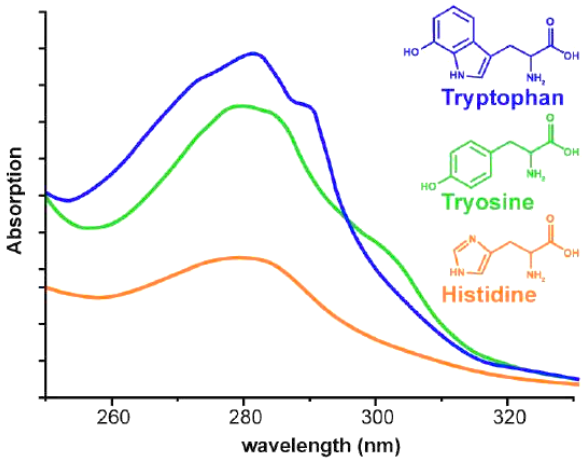


**Figure 33.** The absorption of amino acid tryptophan and tryosine with their chemical structure respectively. Image adapted from [47].

The most common used method to determine the protein concentration in a solution is to measure the absorbance at 280 nm (UV range) because proteins absorb UV-light in proportion to their aromatic amino acid content and total concentration. By following the previous work, we proceed to demonstrate the absorption spectroscopic analysis of CLIC3-HIS tag (Chloride intracellular channel protein 3) human body protein by using the pillar cuvette setup as shown in Fig. 32. This protein is highly expressed in human organs such as lung and heart. CLIC3 protein can insert into membranes and forms ion channels, which means that it may play a role in the regulation of cell growth [48].

Protein quantity is often necessary before processing protein samples for spectroscopic analysis. The CLIC3-HIS proteins are expensive [49], costing $245 for only 10 µg of protein sample. We have access to only 200 µL of pure protein sample volume which is not suitable for performing absorption spectroscopy using a standard cuvette (3.5 mL). For this reason, a miniaturized chip/device is required to detect the proteins and we used a pillar cuvette which requires only 2 µL-3 µL of sample volume. The protein samples used in this study are provided by University of Technology Sydney in falcon tubes with 200 µL of pure protein solution.

The absorption spectroscopy is performed by using a broadband UV-light source to illuminate the transverse section of pillar cuvette and Ocean Optics QE65000 spectrometer has been used to record the broadband spectrum. In order to perform a complete analysis of absorption by CLIC3-HIS tag protein, a buffer solution was used as a reference solution. The buffer solution is prepared by mixing HEPES and KCl solution with concentration 200 mM and 100 nM, respectively.

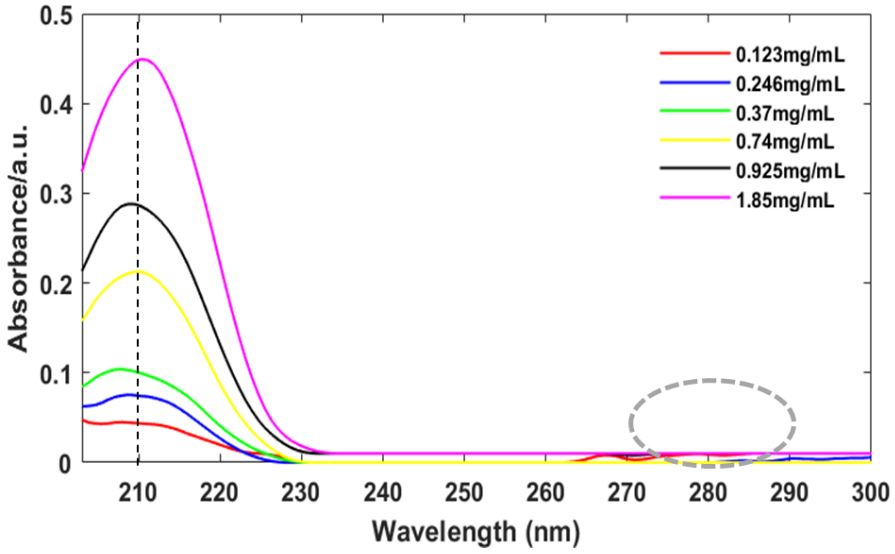


**Figure 34.** Absorption spectrum of CLIC3-HIS protein measured using transverse section of pillar cuvette with optical pathlength of 50 µm. The absorption peak at 210 nm (black dashed line) and no absorption peak observed around 280 nm (grey dashed circle).

The above figure shows the absorption spectrum of CLIC3-HIS protein with concentrations ranging from 0.123 mg/mL to 1.86 mg/mL. The absorption spectrum shows the absorption peak around 210 nm which is due to the contribution of the light absorbed by peptide group of protein [50]. It is evident from the UV-spectrum that the absorption intensity increased regularly (at 210 nm) with increasing concentration of CLIC3-HIS protein according to the Beer Lambert law, as plotted in Fig. 35. From Eq. (2) the slope of following graph presents the value of $\varepsilon l$, which is 0.2522. This way the calculated value for $\varepsilon$ at 220 nm is 50.44 $cm^{-1}mg^{-1}mL$.

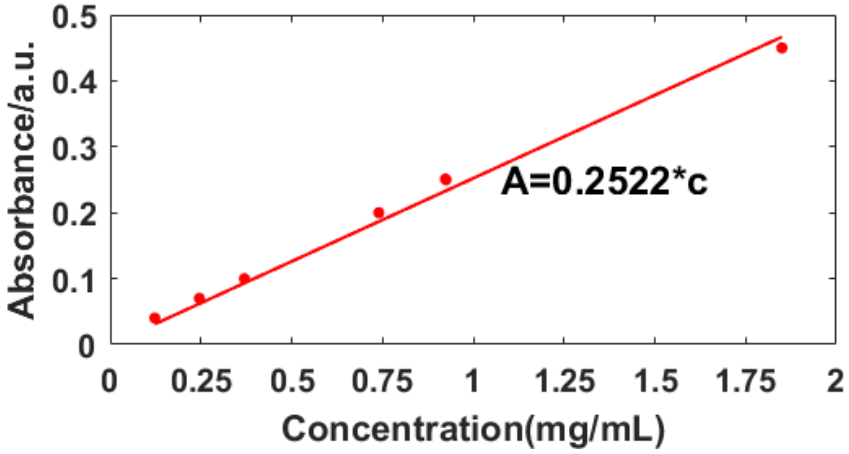


**Figure 35.** Absorbance measured at wavelength 210 nm over the concentration ranging from 0.123 mg/mL to 1.85 mg/mL.

As mentioned above, amino acids present in protein absorb UV light at 280 nm which is not possible to observe at 280 nm in absorption spectrum of Fig. 34 (grey circle). This is due to the low concentration of protein i.e., according to Beer-Lambert law (Eq. 2) absorbance signal is directly proportional to concentration of protein and to optical pathlength of the light interaction with sample. In this case, the optical pathlength is very short (50 μm) which is one of the causes for low absorbance. It is possible to detect the low concentrations if this method is tested with higher optical pathlengths. In protein analysis, most widely used method to determine the unknown concentration of a protein is comparing it to known amounts of the standard protein. Each protein differs in their amino acid compositions, thus their response to spectroscopic analysis is somewhat different in terms of amount of light absorbed at certain wavelengths. Therefore, the best choice for a reference standard is a purified protein with known concentration. If a highly purified version of the protein of interest is unavailable or it is expensive, the alternative is the protein with similar absorbance response curve. As in our case, the purchase of big amount or high concentration of CLIC3-HIS is expensive. For this reason, we chose bovine serum albumin (BSA) protein that works well for as a standard protein. It is widely available with purity and is relatively inexpensive.

The goal is merely to estimate the total CLIC3-HIS tag human body protein concentration that is required to detect the reasonable absorbance signal at 280 nm, and slight protein-to-protein variability is acceptable. BSA is a multipurpose protein derived from bovine blood plasma. The spectroscopic analysis of BSA

protein has been performed by using setup presented in Fig. 32. Fig. 36 shows the absorption spectrum for a concentration ranging from 100 mg/mL to 5 mg/mL. The maximum peak position of BSA was shifted from 205 to 220 nm towards higher wavelength region. The shift in $\lambda_{max}$ could be due to the change in polarity around the tryptophan residue and the change in peptide strand of BSA molecules, hence the change in hydrophobicity [51].

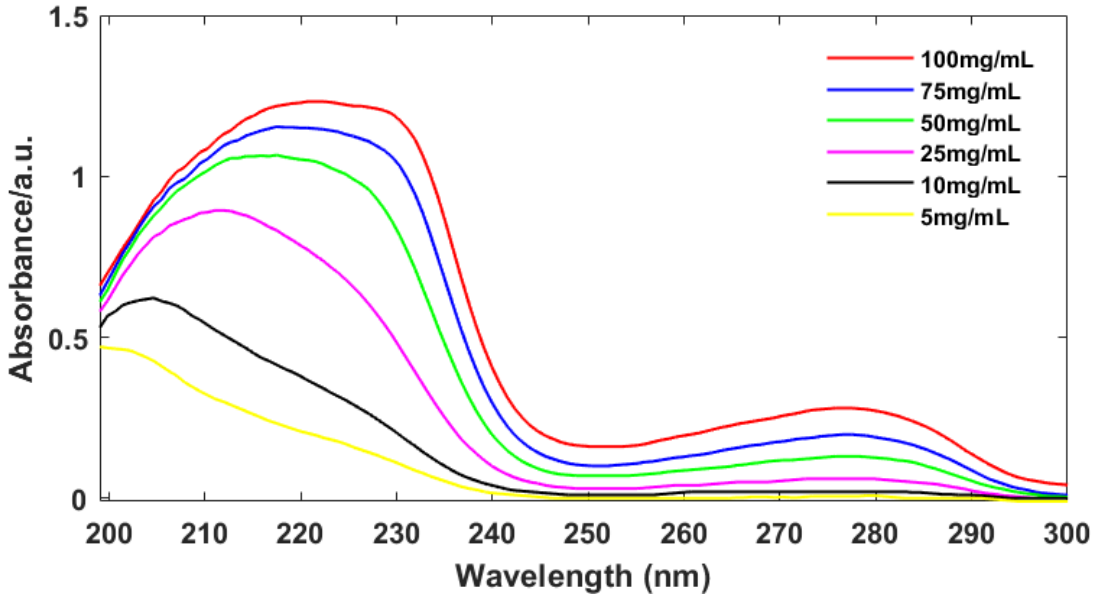


**Figure 36.** Absorption spectrum of BSA protein with optical pathlength of 50 μm using a pillar cuvette in transverse configuration

The calibration curves in Fig. 37 clearly show the linearity of absorbance with protein concentration, according to Eq. (2). The slope of linear regression represents the product of $\varepsilon$ (molar absorptivity) and $l$ (optical pathlength), which is 0.00249. This value was divided by optical pathlength ($l = 50\ \mu m$) such that the molar absorptivity can be determined as, $\varepsilon \approx 0.049\ mL.mg^{-1}mm^{-1} = 33.06\ M^{-1}cm^{-1}$ (at 280 nm). This is slightly lower than the reported value in the literature (i.e. $\lambda = 280\ nm, \varepsilon = 43.82\ M^{-1}cm^{-1}$) [52].

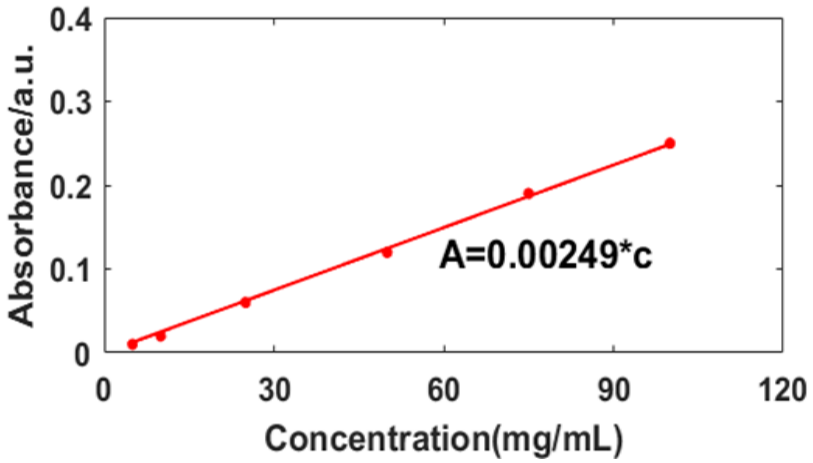


**Figure 37.** Plot of absorbance at a wavelength of 280 nm against the concentration of BSA protein.

The CLIC3-HIS tag protein and BSA protein have similar spectroscopic properties which means the molar absorptivity ($\varepsilon$) of BSA protein at 280 nm can be used to predict the pathlength and CLIC3-HIS concentration values to obtain the peak at 280 nm. From the analysis of the above graphs, it is possible to conclude that the required concentration of CLIC3-HIS protein to observe absorbance peak at 280 nm is higher than 5 mg/mL. It is a big challenge to purchase high concentration human body proteins, due to their cost and unviability at commercial platforms.

To overcome this challenge, we proposed to increase the optical pathlength which will increase the absorbance according to Beer Lambert law. The next section of this thesis presents a new configuration of pillar cuvette with increased optical pathlength. This process will involve the GIF tips and a very similar setup of excitation and collection fibres is used as presented previously in recently developed optofluidic device.

## 5.3. Cross-section Pillar Cuvette Absorption Spectroscopy

In this section, we present a new configuration and setup with pillar cuvettes to perform absorption spectroscopy. This is a compact and real-time absorption spectroscopy setup designed with a focus on taking spectroscopic readings in a microfluidic channel. The innovation in this new configuration is to use the pillar cuvette concept, but probing across the long axis. The proposed setup is illustrated in Fig. 38 which presents the excitation and collection fibre aligned to the pillar cuvette through the longitudinal cross-section.

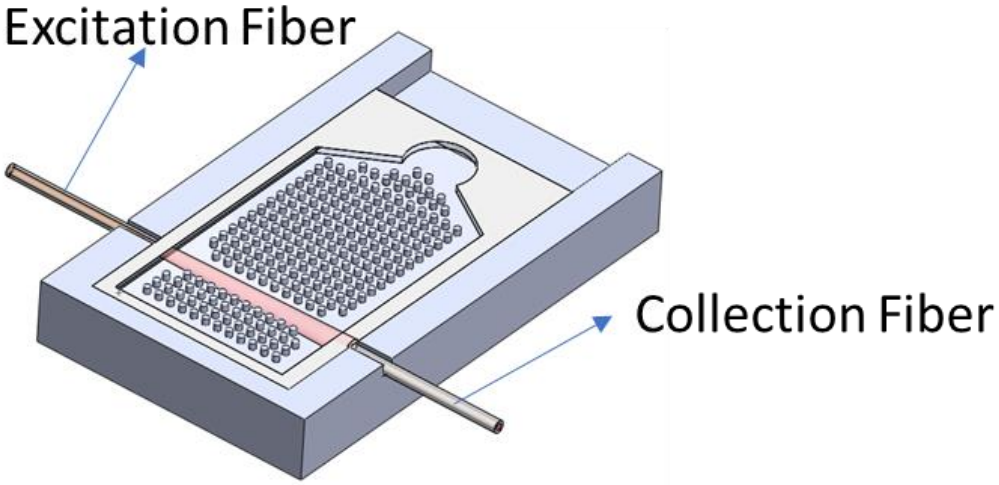


**Figure 38.** Pillar cuvette placed in a holder to align both of the fibers across the long axis.

The two rows of pillars are removed to create a light path. The collimated beam is transmitted longitudinally through the cross-section of the micropillar array that is a pillar cuvette and is collected at the other end. The width of the pillar cuvette defines the optical path length (~6 mm). The main objective of this configuration compared to the setup presented in previous section is a 120-fold increase in the optical pathlength, which will result in high absorbance for low range of concentrations according to Eq. (2). For this application, the GIF tips allow for the development of a highly effective lab-on-a-chip absorption spectroscopy platform that is compact, fibre connectorized and does not require free-space optics, as shown in the below image.

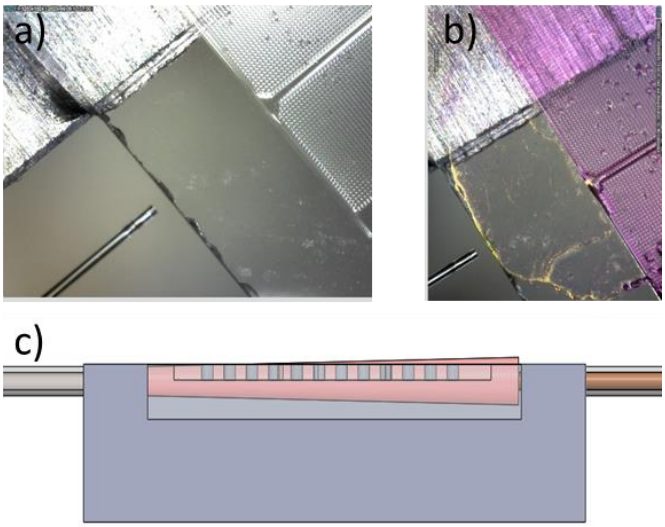


**Figure 39.** a) The alignment of GIF fibre with pillar cuvette cross-section. b) Pillar cuvette filled with liquid solution. c) Side view of pillar cuvette to represent the fibre alignment with pillars.

The setup presented in the above images is very simple but it has critical alignment issues between the fibres and pillar cuvette. The fibre core (responsible for carrying the light) has a 8 µm size and the pillars have 50 µm height in this setup. Due to micro-scale height of pillars and micro-scale core of optical fibres, it requires very precise and accurate equipment to precisely hold the fibre and pillar cuvette. This way both fibres can be properly aligned with the pillars. It is very important to ensure the quick replacement of pillar cuvette without realignments between the measurement.

## 5.3.1. Proposed Solutions – Pillar Cuvette Holder

To overcome the alignment issues, we choose to design an integrated and compact platform to hold optical fibres and allow the pillar cuvette alignment to be maintained when changing cuvettes over. Here we show a novel and fully integrated system relying on a miniaturized platform as shown in the images below. Fig. 40 presents the two holders designed in Solidworks: a) holder with collection fibre (MMF) and pillar cuvette and b) holder with collection and excitation fibre (GIF) and pillar cuvette. Our goal was to design a platform in which a free moving pillar cuvette can be easily integrated with optical fibres and fibres should be aligned to focus and collect the light from the pillar cuvette.

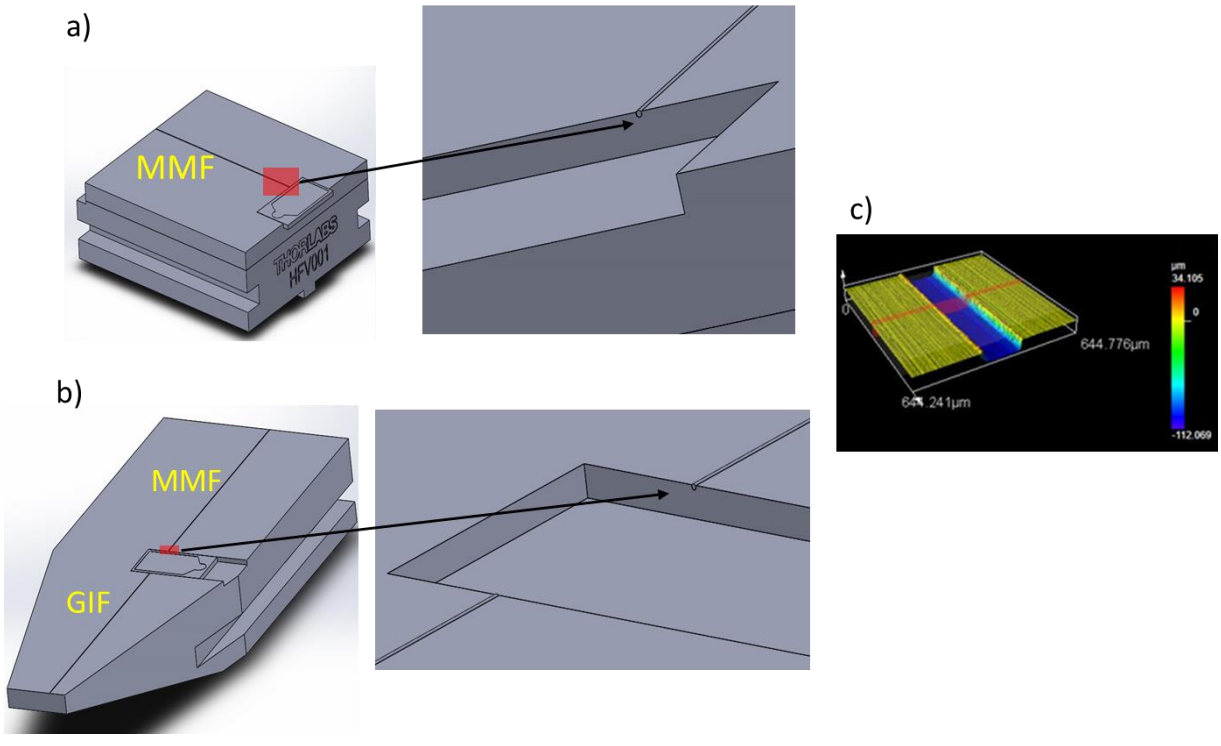


**Figure 40.** Solidworks designs of stainless-steel holder for a) pillar cuvette integrated with collection fibre b) pillar cuvette integrated with GIF and MMF fibre on same platform and c) the fibre groove design and topography.

The basis of this setup is to create a straight rectangular groove machined into a stainless-steel fibre holder from Thorlabs (HFV001 and HFV002). The machined rectangular grooves hold the optical fibres perpendicular to ensure that fibre is perpendicular to pillar cuvette. The fibres can be placed manually into the grooves and both the fibres can be easily aligned to the 50 um pillars of the pillar cuvette where sample flows. The grooves for fibres and pillar cuvette groove are machined using a super milling machine (Kira SuperMill 2M, Japan) at the Australian National Fabrication Facility (ANFF). The optical fibre for the collection was chosen to be multimode fibre (MMF) since they enable large numerical aperture. Therefore, their cylindrical size is slightly bigger which results in a bigger groove for the collection fibre.

These arrangements present some advantages such as easy and precise alignment of the excitation fibre (GIF) and collection fibre (MMF) which avoids alignment issues faced using 6-axis stages. The alignment is important since multiple analytes are detected and for this reason the realignment between measurements needs to be avoided to assure the same parameters for comparison. Due to all these qualities this compact platform can be easily integrated on lab-on-a chip platform.

The next phase of this research is to test the fabricated holders for fibres and pillar cuvette. The future work involves the on-chip absorption spectroscopy of biochemicals such as CLIC3-HIS tag protein, using a supercontinuum laser and GIF tips fibres to show the novelty of a compacted optofluidic device.

# Chapter 6

# Conclusions

In conclusion, this thesis has presented chip-scale optofluidic devices for applications in the biomedical field. First, we have developed a simple optofluidic device to show the potential of GIF tips for integration into a lab-on-a chip platform. The GIF tips with appropriate segment lengths were chosen according to the collimation length which depends on the microchannel length of the device. The optofluidic device shows identical performance to standard cuvettes for absorption spectroscopy but with a 10-fold reduction in the sample volume required. This is enabled by using GIF tips which collimate the output of an optical fibre and could allow for longer channel lengths to be realized. GIF tips enable demonstration of a highly effective lab-on-a-chip absorption spectroscopy platform that is compact, fibre connectorized, and does not require free-space optics or traditional lenses to create the optical path.

The novelty and importance of GIF fibres was demonstrated with their far field divergence angle and insertion losses performance. The GIF tips allow for a 4-fold reduction in both insertion losses and beam divergence angle when compared with the optofluidic chips using standard SMF. In addition, the GIF tip configuration can achieve 1/4 of the optical losses compared to waveguide integrated optofluidic devices such as those presented by Malic *et al.* [9].

The simple and practical optofluidic device is shown to detect down to 16 μM concentration of thiocyanate in artificial saliva, which is more than sufficient for the quantitative measurement of SCN in saliva for the purpose of identification of irregularities in saliva. Thiocyanate being an important component in saliva that has been demonstrated as a chemical indicator for oral health and a detoxification product for cancer treatments.

Second, we have presented another optofluidic device based on pillar cuvettes with high feasibility for integration into LOC platform. The cross-section configuration of pillar cuvette with GIF tips was developed to monolithically integrate the pillar cuvette with V-groove for fibre alignment scheme. The direct comparison of cross-section configuration to 50 μm pathlength experiment setup is 120-fold increase in optical pathlength. This clearly points out that a simple and compact cross-section experimental setup can result in a small-scale optofluidic device which will be competitive with the most advanced integrated photonics devices.

To our knowledge, these are the first optofluidic sensors for absorption spectroscopy which are based on GIF tip fibres. These devices could be easily integrated for lab-on-a-chip devices or implemented for highly sensitive cavity-enhanced absorption technologies. Some modifications can further improve performance of the system and its ease of use.

For the future work, the benefits of using optofluidic devices based on pillar cuvette microchips will be explored including:

a) The use of integrated GIF tips as the excitation fibre and MMF for collection in the detection system allowing simultaneous multianalyte detection and increased system throughput. Furthermore,

monolithic integration of the optical fibres with the microfluidic chip (pillar cuvette) provides precise alignment of the optical components and inherent system stability.

b) Integration of a V-groove fibre coupling method on chip allows system portability and reduces alignment time and cost.

c) As shown in Fig. 30 the fabrication steps are fully automated and thus this could be suitable for mass production of these devices for the LOC platform.

The presented device design can be optimized to minimize the coupling losses between the optical fibres and the pillar cuvette under the imposed fabrication constraints. However, further optimization of the GIF tips with the same fabrication methods and materials is possible.

# References


[1] O. Axner, F. M. Schmidt, A. Foltynowicz, J. Gustafsson, N. Omenetto, and J. D. Winefordner, "Absorption spectrometry by narrowband light in optically saturated and optically pumped collision and Doppler broadened gaseous media under arbitrary optical thickness conditions," *Applied spectroscopy,* vol. 60, no. 11, pp. 1217-1240, 2006.

[2] H. Becker and L. E. Locascio, "Polymer microfluidic devices," *Talanta,* vol. 56, no. 2, pp. 267-287, 2002.

[3] P. Minzioni *et al.*, "Roadmap for optofluidics," *Journal of Optics,* vol. 19, no. 9, p. 093003, 2017.

[4] A. Manz, N. Graber, and H. á. Widmer, "Miniaturized total chemical analysis systems: a novel concept for chemical sensing," *Sensors and actuators B: Chemical,* vol. 1, no. 1-6, pp. 244-248, 1990.

[5] J. Wu, "Development of integrated optofluidic sensors," Degree of Philosophy Centre for Micro-photonics, Swinburne University of Technology, Melbourne, Australia, 2009.

[6] S. K. Tiwari, S. Bhat, and K. K. Mahato, "Design and fabrication of low-cost microfluidic channel for biomedical application," *Scientific Reports,* vol. 10, no. 1, pp. 1-14, 2020.

[7] D. Psaltis, S. R. Quake, and C. Yang, "Developing optofluidic technology through the fusion of microfluidics and optics," *nature,* vol. 442, no. 7101, pp. 381-386, 2006.

[8] G. B. Loozen, A. Karuna, M. M. Fanood, E. Schreuder, and J. Caro, "Integrated photonics multi-waveguide devices for optical trapping and Raman spectroscopy: design, fabrication and performance demonstration," *Beilstein journal of nanotechnology,* vol. 11, no. 1, pp. 829-842, 2020.

[9] L. Malic and A. G. Kirk, "Integrated miniaturized optical detection platform for fluorescence and absorption spectroscopy," *Sensors and Actuators A: Physical,* vol. 135, no. 2, pp. 515-524, 2007.

[10] T. Ngernsutivorakul *et al.*, "Design and microfabrication of a miniature fiber optic probe with integrated lenses and mirrors for Raman and fluorescence measurements," *Analytical and bioanalytical chemistry,* vol. 409, no. 1, pp. 275-285, 2017.

[11] L. Ali, M. U. Mohammed, M. Khan, A. H. B. Yousuf, and M. H. Chowdhury, "High-Quality Optical Ring Resonator-Based Biosensor for Cancer Detection," *IEEE Sensors Journal,* vol. 20, no. 4, pp. 1867-1875, 2019.

[12] C. Song and S. H. Tan, "A Perspective on the Rise of Optofluidics and the Future," *Micromachines,* vol. 8, no. 5, p. 152, 2017.

[13] D. Harvey. "Absorbance and Emission Spectroscopy." Image and Video Exchange Forum. (accessed 02 December, 2020).

[14] I. Rodríguez-Ruiz, T. N. Ackermann, X. Muñoz-Berbel, and A. Llobera, "Photonic lab-on-a-chip: Integration of optical spectroscopy in microfluidic systems," ed: ACS Publications, 2016.

[15] S. R. Neil, C. M. Rushworth, C. Vallance, and S. R. Mackenzie, "Broadband cavity-enhanced absorption spectroscopy for real time, in situ spectral analysis of microfluidic droplets," *Lab on a Chip,* vol. 11, no. 23, pp. 3953-3955, 2011.

[16] C. M. Rushworth, G. Jones, M. Fischlechner, E. Walton, and H. Morgan, "On-chip cavity-enhanced absorption spectroscopy using a white light-emitting diode and polymer mirrors," *Lab on a Chip,* vol. 15, no. 3, pp. 711-717, 2015.

[17] A. Nitkowski, L. Chen, and M. Lipson, "Cavity-enhanced on-chip absorption spectroscopy using microring resonators," *Optics express,* vol. 16, no. 16, pp. 11930-11936, 2008.

[18] S. M. Ball, J. M. Langridge, and R. L. Jones, "Broadband cavity enhanced absorption spectroscopy using light emitting diodes," *Chemical Physics Letters,* vol. 398, no. 1-3, pp. 68-74, 2004.

[19] Z. Ding, Y. Zhao, H. Ren, J. S. Nelson, and Z. Chen, "Real-time phase-resolved optical coherence tomography and optical Doppler tomography," *Optics Express,* vol. 10, no. 5, pp. 236-245, 2002.
[20] B. Du *et al.*, "In-Fiber collimator-based Fabry-Perot interferometer with enhanced vibration sensitivity," *Sensors,* vol. 19, no. 2, p. 435, 2019.
[21] S. Bi *et al.*, "Influence of no-core fiber on the focusing performance of an ultra-small gradient-index fiber probe," *Optics and Lasers in Engineering,* vol. 107, pp. 46-53, 2018.
[22] M. C. Fenta, D. K. Potter, and J. Szanyi, "Fibre optic methods of prospecting: A comprehensive and modern branch of geophysics," *Surveys in Geophysics,* vol. 42, no. 3, pp. 551-584, 2021.
[23] "https://en.wikipedia.org/wiki/File:Optical-fibre.png." (accessed 06 June, 2021).
[24] M. Zickar, W. Noell, C. Marxer, and N. de Rooij, "MEMS compatible micro-GRIN lenses for fiber to chip coupling of light," *Optics express,* vol. 14, no. 10, pp. 4237-4249, 2006.
[25] C. Wang, C. Fang, Z. Tang, Y. Yu, Y. Mao, and B. Qi, "Analytical method for designing gradient-index fiber probes," *Optical Engineering,* vol. 50, no. 9, p. 094202, 2011.
[26] D. Lorenser, X. Yang, and D. D. Sampson, "Accurate modeling and design of graded-index fiber probes for optical coherence tomography using the beam propagation method," *IEEE Photonics Journal,* vol. 5, no. 2, pp. 3900015-3900015, 2013.
[27] P. Micro-optics. "https://www.pmoptics.com/." (accessed 14/10/2020)).
[28] I. H. Malitson, "Interspecimen comparison of the refractive index of fused silica," *Josa,* vol. 55, no. 10, pp. 1205-1209, 1965.
[29] N. Riesen, N. Phillips, and D. G. Lancaster, "Design guidelines for collimating or focusing graded-index fiber tips," *Optics Express,* vol. 29, no. 19, pp. 29982-29995, 2021.
[30] Queen. "https://queen.com.au/product/pillar-box-red-food-colour-50ml/." (accessed 13/11/2020, 2020).
[31] Milli-Q. "https://www.merckmillipore.com/GB/en/product/Milli-Q-Reference-Water-Purification-System,MM_NF-C79625." (accessed 11/11/2020, 2020).
[32] K. Bevziuk, A. Chebotarev, D. Snigur, Y. Bazel, M. Fizer, and V. Sidey, "Spectrophotometric and theoretical studies of the protonation of Allura Red AC and Ponceau 4R," *Journal of Molecular Structure,* vol. 1144, pp. 216-224, 2017.
[33] V. Arya, M. De Vries, K. A. Murphy, A. Wang, and R. O. Claus, "Exact analysis of the extrinsic Fabry-Perot interferometric optical fiber sensor using Kirchhoff's diffraction formalism," *Optical Fiber Technology,* vol. 1, no. 4, pp. 380-384, 1995.
[34] M. F. Erdoğan, "Thiocyanate overload and thyroid disease," *Biofactors,* vol. 19, no. 3-4, pp. 107-111, 2003.
[35] A. Phonchai, T. Srisukpan, S. Riengrojpitak, P. Wilairat, and R. Chantiwas, "Simple and rapid screening of the thiocyanate level in saliva for the identification of smokers and non-smokers by capillary electrophoresis with contactless conductivity detection," *Analytical Methods,* vol. 8, no. 25, pp. 4983-4990, 2016.
[36] J. Flieger, J. Kawka, and M. Tatarczak-Michalewska, "Levels of the Thiocyanate in the Saliva of Tobacco Smokers in Comparison to e-Cigarette Smokers and Nonsmokers Measured by HPLC on a Phosphatidylcholine Column," *Molecules,* vol. 24, no. 20, p. 3790, 2019.
[37] K. de Berg, M. Maeder, and S. Clifford, "A new approach to the equilibrium study of iron (III) thiocyanates which accounts for the kinetic instability of the complexes particularly observable under high thiocyanate concentrations," *Inorganica Chimica Acta,* vol. 445, pp. 155-159, 2016.
[38] H. S. Frank and R. L. Oswalt, "The stability and light absorption of the complex ion FeSCN++," *Journal of the American Chemical Society,* vol. 69, no. 6, pp. 1321-1325, 1947.
[39] S. Gao, S. Gao, B. Xu, and H. Yu, "Effects of different pH-values on the nanomechanical surface properties of PEEK and CFR-PEEK compared to dental resin-based materials," *Materials,* vol. 8, no. 8, pp. 4751-4767, 2015.

[40] C. V. Kalburgi, K. L. Naik, M. V. Kokatnur, and S. Warad, "Estimation and correlation of salivary thiocyanate levels in healthy and different forms of tobacco users having chronic periodontitis: A cross-sectional biochemical study," *Contemporary clinical dentistry,* vol. 5, no. 2, p. 182, 2014.

[41] L. Wu, Z. Wang, S. Zong, and Y. Cui, "Rapid and reproducible analysis of thiocyanate in real human serum and saliva using a droplet SERS-microfluidic chip," *Biosensors and Bioelectronics,* vol. 62, pp. 13-18, 2014.

[42] R. K. Bhandari *et al.*, "Simultaneous determination of cyanide and thiocyanate in plasma by chemical ionization gas chromatography mass-spectrometry (CI-GC-MS)," *Analytical and bioanalytical chemistry,* vol. 404, no. 8, pp. 2287-2294, 2012.

[43] G. Holzner, F. H. Kriel, and C. Priest, "Pillar cuvettes: capillary-filled, microliter quartz cuvettes with microscale path lengths for optical spectroscopy," *Analytical chemistry,* vol. 87, no. 9, pp. 4757-4764, 2015.

[44] F. H. Kriel and C. Priest, "Influence of sample volume and solvent evaporation on absorbance spectroscopy in a microfluidic “pillar-cuvette”," *Analytical Sciences,* vol. 32, no. 1, pp. 103-108, 2016.

[45] A. Alrifaiy, O. A. Lindahl, and K. Ramser, "Polymer-based microfluidic devices for pharmacy, biology and tissue engineering," *Polymers,* vol. 4, no. 3, pp. 1349-1398, 2012.

[46] P. Naulleau, "Optical lithography," Lawrence Berkeley National Lab.(LBNL), Berkeley, CA (United States), 2012.

[47] California.University. "https://chem.libretexts.org/Courses/University_of_California_Davis/UCD_Chem_105/UCD_Chem_105%3A_Lab_Manual/Lab_8%3A_Quantifying_Protein_Concentration." Chemistry Libretexts. (accessed 14-May-2021.

[48] Z. Qian, D. Okuhara, M. K. Abe, and M. R. Rosner, "Molecular cloning and characterization of a mitogen-activated protein kinase-associated intracellular chloride channel," *Journal of Biological Chemistry,* vol. 274, no. 3, pp. 1621-1627, 1999.

[49] ElabScience. "https://www.elabscience.com/p-recombinant_human_clic3_protein_his_tag_-106006.html." (accessed 04-December-2020.

[50] M. Pathak *et al.*, "Binding of ethyl pyruvate to bovine serum albumin: Calorimetric, spectroscopic and molecular docking studies," *Thermochimica Acta,* vol. 633, pp. 140-148, 2016.

[51] A. T. Buddanavar and S. T. Nandibewoor, "Multi-spectroscopic characterization of bovine serum albumin upon interaction with atomoxetine," *Journal of Pharmaceutical Analysis,* vol. 7, no. 3, pp. 148-155, 2017.

[52] J. J. Babcock and L. Brancaleon, "Bovine serum albumin oligomers in the E-and B-forms at low protein concentration and ionic strength," *International journal of biological macromolecules,* vol. 53, pp. 42-53, 2013.

# Journal article

## On-chip absorption spectroscopy enabled by graded index fiber tips

**KAMALPREET K. GILL,[1,2] NICOLAS RIESEN,[1,2,3,*] CRAIG PRIEST,[1,2] NICHOLAS PHILLIPS,[1,4] BIN GUAN,[1] AND DAVID G. LANCASTER[1,2]**

[1]*Future Industries Institute and STEM, University of South Australia, Mawson Lakes, SA 5095, Australia*

[2]*ARC Research Hub for Integrated Devices for End-user Analysis at Low-levels (IDEAL), UniSA STEM, University of South Australia, Mawson Lakes, SA 5095, Australia*

[3]*Institute for Photonics and Advanced Sensing and School of Physical Sciences, University of Adelaide, SA 5005, Australia*

[4]*Defence Science and Technology Group, Third Ave, Edinburgh, SA 5111, Australia*

[*]*nicolas.riesen@unisa.edu.au*

**Abstract:** This paper describes the design and characterization of miniaturized optofluidic devices for sensing based on integrating collimating optical fibers with custom microfluidic chips. The use of collimating graded-index fiber (GIF) tips allows for effective fiber-channel-fiber interfaces to be realized when compared with using highly-divergent standard single-mode fiber (SMF). The reduction in both beam divergence and insertion losses for the GIF configuration compared with SMF was characterized for a 10.0 mm channel. Absorption spectroscopy was demonstrated on chip for the measurement of red color dye (Ponceau 4R), and the detection of thiocyanate in water and artificial human saliva. The proposed optofluidic setup allows for absorption spectroscopy measurements to be performed with only 200 µL of solution which is an order of magnitude smaller than for standard cuvettes but provides a comparable sensitivity. The approach could be integrated into a lab-on-a-chip system that is compact and does not require free-space optics to perform absorption spectroscopy.



# 1. Introduction

Optofluidics is a rapidly growing field that emerged in the early 2000s as the disciplines of nanophotonics and microfluidics matured. It holds promise for the next generation of portable molecular detectors that will ultimately become more important in our everyday life [1,2]. Optofluidics involves the simultaneous control of fluids and optical beams and aims to integrate several optical functions into a single chip in the lab-on-a-chip approach, replacing the need for bulk free-space optics [3]. With the global microfluidics market size currently USD 15.7 billion and projected to reach USD 44.0 billion by 2025 at a compound annual growth rate of 23% and with optofluidics still being in its infancy there exists significant untapped commercial potential for such optics-enriched microfluidic devices [4]. Since most lab-on-a-chip optofluidic devices have been limited to short-term research rather than being directly integrated into user-friendly real-world products, there is a need to focus on simple, practical and cost-effective devices which balance design and real-world impact. This improves the chances of techniques and technologies being developed that can be commercialized.

One of the simpler and more practical on-chip sensing techniques is absorption spectroscopy which can be used to determine the concentration of an analyte of interest through the BeerLambert law, which can be expressed by:

$$A = -\log\left(\frac{I}{I_0}\right) = \varepsilon l c \qquad (2)$$

where $I$ and $I_0$ are the intensities of light transmitted in presence and absence of an analyte, respectively, ε is the molar absorptivity coefficient, $l$ is the optical pathlength and $c$ is the concentration of the analyte in the sample. In previous work, Priest *et al.* [5,6] reported a quartz glass microfluidic chip with a micropillar array (i.e. pillar cuvette) as an effective single-pass absorption measurement platform with only ~2 µL sample volume, but which was limited by a very short interaction length $l$. The literature contains an increasing number of reports which propose optical detection methods that mitigate the problem of short path length, including cavity-enhanced absorption spectroscopy (CEAS) [7,8], and cavity ring-down spectroscopy (CRDS) [9,10]. These optical detection methods have their own advantages and limitations in terms of simplicity, sensitivity and cost. The simplest technique of single-pass absorption spectroscopy is usually limited to short interaction lengths (~mm's) due to the typical divergence of the beams coming from standard fibers or laser-written waveguides which limit the possible channel length because of the increased coupling losses [11].

In this paper we make significant inroads into increasing the interaction length for single-pass absorption spectroscopy by using lensed graded-index fiber (GIF) tips. GIF tips have found significant use in recent years in optical coherence tomography (OCT) biomedical imaging and micro-electromechanical system (MEMs) applications but have only seen limited use outside of these fields [12–15]. GIF tips have also recently found use in interferometric Fly-paper sensors [16–18]. In this paper the GIF tips enable demonstration of a highly effective lab-on-a-chip absorption spectroscopy platform that is compact, fiber connectorized, and does not require free-space optics or traditional lenses to create the optical path. The GIF tips have a collimated output that is transmitted longitudinally through a custom fabricated microchannel and is collected by a multimode fiber at the other end. These GIF tips can easily be incorporated into optofluidic assemblies. In addition, the GIF tip configuration can achieve 1/4 of the optical losses compared to waveguide integrated optofluidic devices such as those presented by Malic *et al.* [11].

We demonstrate that this device can allow for absorption spectroscopy to be undertaken with sample volumes ten times smaller than standard cuvettes but with similar sensitivity. This is particularly relevant for microvolume samples containing analytes such as proteins or antibodies. A proof-of-concept detection of a biologically relevant analyte, thiocyanate, in artificial human saliva, is also presented. Moreover, advanced fabrication techniques such as photolithography could be used to achieve nL volumes [7–9,11].

# 2. Experimental setup

## 2.1. GIF tips

The GIF tips used here consist of three fiber sections spliced together as shown in Fig. 1. The incoming fiber is single-mode fiber (SMF), followed by a coreless fiber (CF) segment that expands the beam. The beam then enters a graded-index fiber segment, which collimates it.

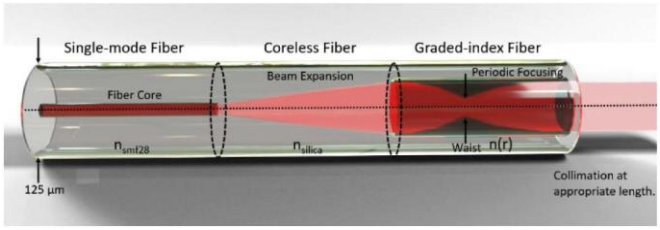


**Fig. 1.** Schematic of GIF tip composed of a single-mode fiber spliced to a mode expanding coreless fiber, which is spliced to a graded-index fiber. Figure adapted from [19].

In this work we used Nufern GF1 single-mode fiber (NA=0.13), Thorlabs FG125LA coreless fiber and Thorlabs GIF625 graded-index fiber. Appropriate segment lengths for minimizing the far-field divergence angle were derived (coreless segment ~ 200 µm, graded-index segment ~ 100 µm) using an optimization routine in which the coreless and graded-index fiber lengths were scanned over a large parameter space using RSOFT BeamProp. Figure 2 shows the contour plot of the far-field divergence angle (in degrees) as a function of coreless and graded-index segment lengths, that was used for optimizing the GIF tips at 532 nm. For this simulation the fundamental mode in the Nufern GF1 fiber was used. Slight variations in the beam divergence can be expected if higher-order modes are excited in the GF1 fiber. The beam divergence for the optimized GIF tip (1.31°) is much lower than for SMF28 fiber (4.6°) at λ=532 nm. The GIF tips were fabricated by splicing 218 µm and 91 µm lengths of coreless and graded-index fiber segments, respectively, to the end of the GF1 single-mode fiber. The fabrication process involves precise thickness steel shims used in a straightforward process we have developed around a standard commercial cleaver/splicer combination. In terms of repeatability, the fabrication tolerances for the lengths of the fiber segments were approximately ±10 microns, using the steel shims that achieve the required fiber lengths when splicing together the coreless and graded-index fiber sections to the single mode fiber.

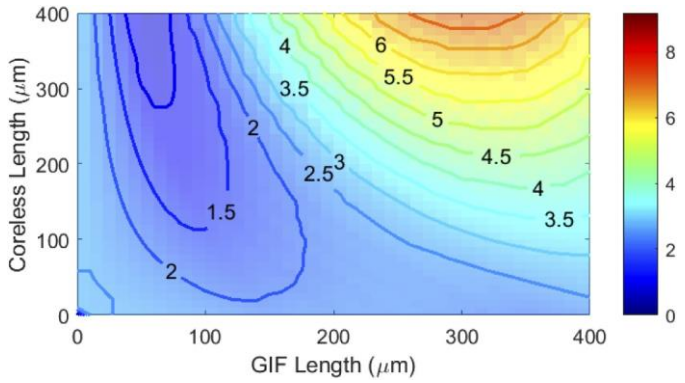


**Fig. 2.** Contour plot of far-field divergence angle of GIF tips (in degrees) as a function of coreless and graded-index fiber segment lengths at λ=532nm. Fundamental mode launch in the GF1 fiber is simulated.

At this point it is worth noting that whilst GF1 and SMF28 fibers are classified and referred to as single-mode fibers, they are actually few-moded at visible wavelengths. This can have some minor influence on the beam divergence of both GIF tips and SMF fibers, although the launch conditions can be tweaked to ensure predominately fundamental mode excitation.

## 2.2. Microfluidic device

The microfluidic chip shown in Fig. 3 was fabricated using glass chips and precision v-grooves (sub-micron accuracy) for holding and aligning the fiber ends. These components were bonded together using NOA65 UV-curing adhesive to create a ~200 µL microchannel. To enhance single-pass absorption spectroscopy measurements within the microfluidic chip, the fabricated GIF tip (excitation fiber) was aligned to a Thorlabs M137L03 200 µm core multimode fiber (collection fiber) using the two spaced v-grooves (127 µm pitch). After precise insertion of the fibers into the v-grooves, the fibers were fixed using the UV-curable optical adhesive. The length of the channel between the excitation fiber and the collection fiber defines the optical path length which in this case was 10.0 mm. To assess the performance of the optofluidics cuvette (volume 3.5 mL) in a standard setup using the same input source as the microfluidic device as shown in Fig. 4(a).

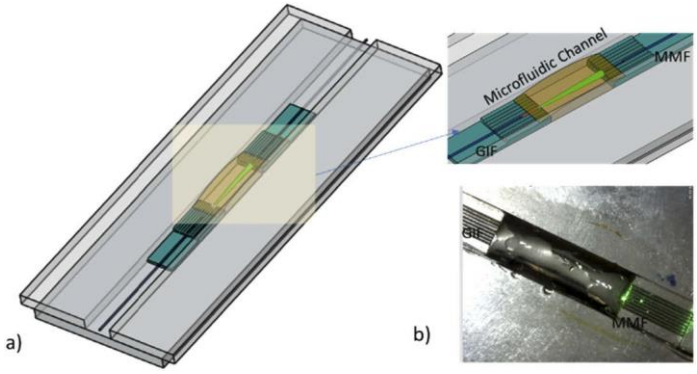


**Fig. 3.** (a) Device design showing microfluidic channel and GIF tip aligned to MMF within v-grooves (b). Close-up of channel.

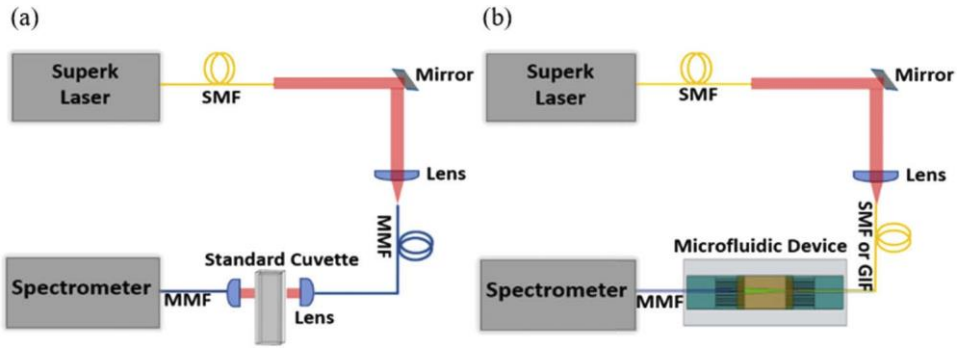


**Fig. 4.** Experimental setup for absorption measurements with (a) standard cuvette and (b) microfluidic device.

## 2.3. Absorption spectroscopy setup

To measure absorption spectra, a broadband supercontinuum laser (YSL Photonics SC-OEM) was used as the excitation source in addition to a monochromator (iHR550, Horiba, Japan) equipped with three different gratings; 600, 1200, and 2400 $mm^{-1}$ and a cooled CCD (Synapse 2048 pixels, Horiba, Japan). The Horiba iHR550 monochromator was used for detection in both the standard cuvette and microfluidic device setups. The experimental setup is illustrated in Fig. 4 for the (a) 10.00 mm width standard cuvette and the (b) custom microfluidic device.

The standard cuvette setup required traditional lenses to collimate the output beam of the MMF (excitation fiber) and to focus the beam in the receiving MMF (collection fiber). In the case of the microfluidic device, the collimated beam is directed longitudinally through the microchannel and collected by the multimode fiber at the other end. The standard cuvette and GIF-enabled microfluidic chips were compared for a range of analytes including red food colour dye (Ponceau 4R Food Color), thiocyanate in water and in artificial human saliva.

The artificial human saliva was prepared based on the composition of the SAGF medium with minor modification [20]. This involved mixing sodium chloride (125mg), potassium chloride (964mg), calcium chloride dihydrate (228mg), potassium phosphate monobasic (655mg), urea (200mg), sodium bicarbonate (631mg), disodium sulfate decahydrate (763mg) and ammonium chloride (178mg) in 1 L of MilliQ water. Different amounts of sodium thiocyanate were added to prepare a series of thiocyanate concentrations. For this experiment the beam divergence of the GIF and SMF were measured using an Ophir Spiricon silicon-based CCD camera. To ensure predominantly single-mode operation the launch conditions were tweaked for the SMF fibers. To study the coupling and transmission losses between SMF-MMF and GIF-MMF fibers as a function of channel length, an optical power meter (Thorlabs S120C, PM100D) was used.

# 3. Results and discussion

In this section we demonstrate the operation of the microfluidic device using a simple solution of red color dye. Absorption spectroscopy is then demonstrated for iron (III) thiocyanate $Fe(SCN)^{2+}$ prepared in water. Finally, the sensing platform is shown for the specific application of detecting the thiocyanate biomarker in artificial human saliva.

## 3.1. Red color dye

The absorption of the red food color dye at its absorption peak of 501nm is shown in Fig. 5 as a function of dye concentration (5µM to 33µM) for both the standard cuvette and the custom GIF-enabled microfluidic chip. The absorption spectrum measured using the supercontinuum source is given for all concentrations in the inset of Fig. 5.

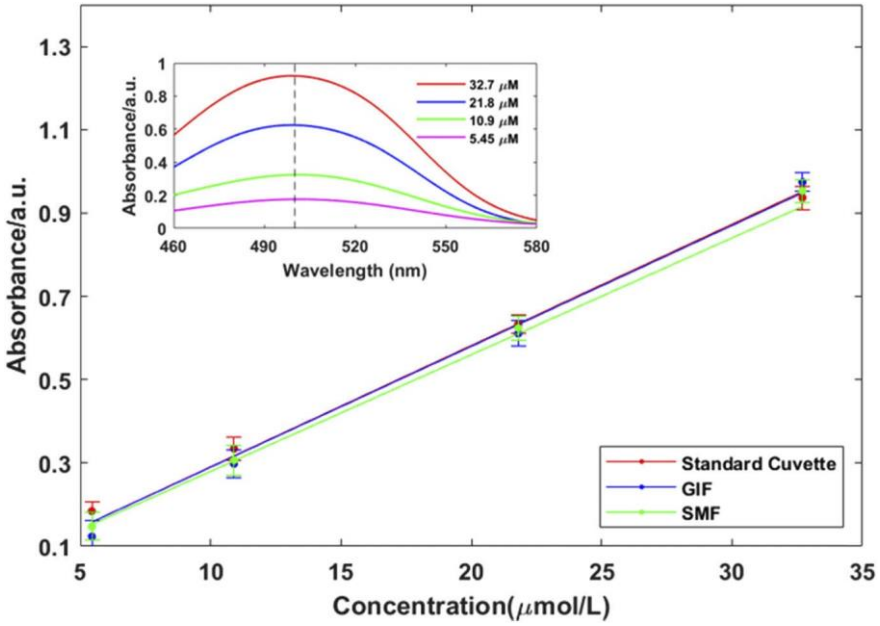


**Fig. 5.** Plot of absorbance at 501nm of red color dye for a standard cuvette (A=0.029C) and the microfluidics chip with either GIF tip (A=0.029C) or SMF fiber (A=0.029C). The inset shows the absorption spectra of concentrations ranging from 5.45 µmol/L to 32.7 µmol/L.

To mitigate the effect of laser instability, the transmitted power $I$ for each measurement is normalized to the power recorded prior to filling the microchannel with the analyte. The absorbance measurements at each concentration, $A$, were obtained by taking the ratio of the normalized transmitted power $I$ to the power $I_o$ recorded in absence of the analyte of interest. The calibration curves in Fig. 5 clearly show the linearity of absorbance with dye concentration, according to the Beer-Lambert law, Eq. (1). The molar absorptivity value is $\varepsilon \approx 28{,}891\ L.mol^{-1}cm^{-1}$, which is in agreement with literature [21]. The quantitative analysis shows the ability to reproduce linearity using a microfluidic device with only ~200µL of solution compared with the 3.5mL standard cuvette, while maintaining the same interaction length. This is particularly noteworthy given that only small sample volumes are commonly accessible in point-of-care diagnostics. Although the microfluidic device absorbance results are comparable when using the standard SMF28 fiber and the GIF tip, the significantly higher beam divergence of SMF means there is lower collection efficiency at the MMF. For this reason, higher power is required in the SMF compared to the GIF tip to achieve similar signal to noise ratios. The far-field divergence angle of both fibers is shown in Fig. 6(a). The GIF tip presents a near-collimated beam of 1.31° far-field divergence angle, which is approximately 4× lower than the 4.6° far-field divergence angle for SMF28 fiber at 532 nm. Figure 6(b) compares the diverging beam radius of the SMF and the GIF tip as a function of propagation distance at wavelengths of 532 nm and 650

nm. As predicted, the beam divergence is relatively insensitive to wavelength changes of the order of ~100 nm.

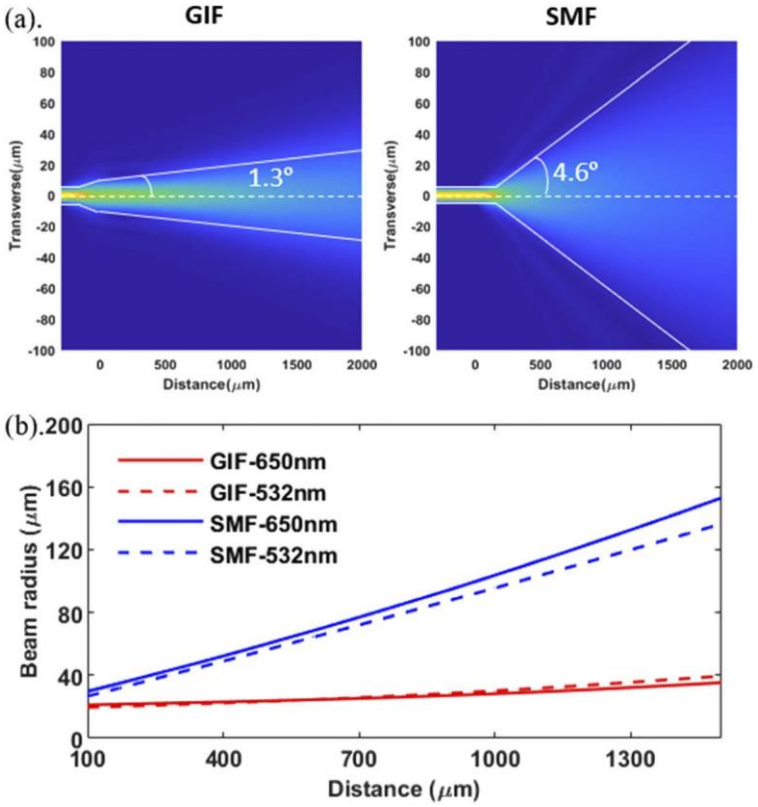


**Fig. 6.** (a). The beam divergence angle of SMF28 and the GIF tip (coreless fiber segment=218 μm and graded-index segment=91 μm). (b) Measured beam radius of SMF28 (blue curves) and GIF tip (red curves) as a function of propagation distance at 532nm and 650nm.

The comparison of SMF-MMF and GIF-MMF coupling efficiencies is shown in Fig. 7. The graph shows that for a fixed distance between the excitation and collection fibers (10.0 mm) the optical losses can be 15× lower when using the GIF tip fiber. This effectively means the GIF setup could be used for significantly longer channels for a given permissible insertion loss. In addition, the GIF setup has 4× less optical losses compared to waveguide integrated optofluidic devices presented by for example Malic *et al*. [11].

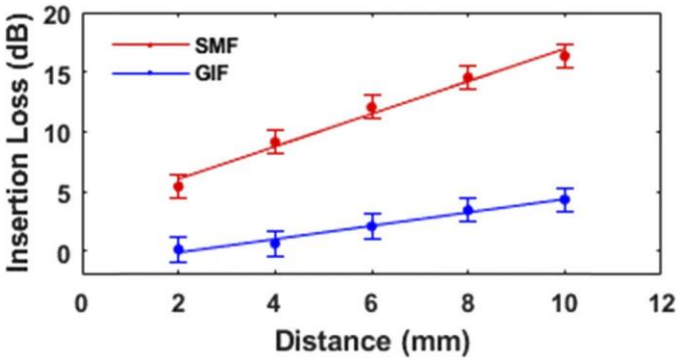


**Fig. 7.** Measured insertion losses of GIF-MMF and SMF-MMF configurations.

The low insertion losses also mean that lower power can be used for a given channel length, avoiding potential issues such as bleaching of the sample when higher powers are required. This shows the significant benefits of using GIF tips in fiber connectorized lab-on-a-chip spectroscopic applications.

## 3.2. Thiocyanate in water

To further demonstrate this optofluidic setup, we show that it can be used for detection of biologically-relevant analytes such as thiocyanate. Thiocyanate ($SCN^-$) was chosen as it is of particular interest in medical diagnostics [22], because it is a detoxification product of cancers and an indicator of oral health including exposure to passive smoking [23]. The complexation reaction between the Fe (III) ions and $SCN^-$ ligands (non-metal) forms a red-orange color compound, $Fe(SCN)^{2+}$, which allows for color techniques such as absorption spectroscopy to be used for its detection Absorption measurements at 480 nm (close to the 460 nm absorption peak of $Fe(SCN)^{2+}$ but far enough away from the supercontinuum wavelength cut-off) were performed using the same setup as before, mixing in 1:1 ratio by volume various $SCN^-$ concentrations (50 µM to 410 µM) with a 26.4 mM concentration of Fe(III)), and a 1:1 mixture of the Fe(III) solution and water was used as the reference. Note that after mixing the $SCN^-$ solution with the Fe(III) solution, fading of the color over time occurs [24]. To avoid this the absorbance measurements were performed immediately after mixing the two reagents. The uncertainty in the measurements was determined from the standard deviation of 10 measurements taken of the spectrum over a duration of 100 seconds. Figure 8 shows the absorption spectra and the absorbance as a function of the $SCN^-$concentration for the three configurations described, with the results showing comparable linearity according to the Beer-Lambert Law. Based on the Beer-lambert law the molar absorptivity of $Fe(SCN)^{2+}$ at the wavelength of 480 nm can be determined as, $\varepsilon \approx 2389\ L.mol^{-1}cm^{-1}$. This is lower than the reported value in the literature (i.e. $\lambda$=480 nm, $\varepsilon$=3914 L. $mol^{-1}\,cm^{-1}$; $\lambda$=500 nm, $\varepsilon$=2900 $L.mol^{-1}\,cm^{-1}$ with ionic strength being 0.5) [25], most likely due to the lower ionic strength in our solutions (i.e. 0.1) compared to that used in the literature.

## 3.3. Thiocyanate in artificial saliva

We also explore the GIF tip enabled optofluidic setup for thiocyanate detection in a more complicated sample matrix other than water, artificial saliva, underpinning its potential for

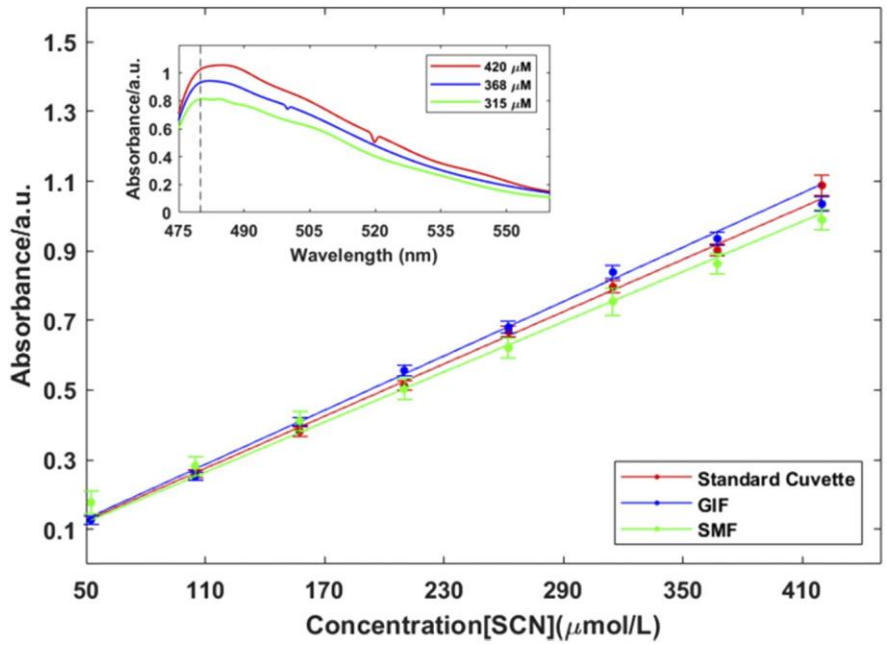


**Fig. 8.** Plot of absorbance at 480nm for $Fe(SCN)^{2+}$ solution as a function of $SCN^-$ concentration in water for standard cuvette (A=0.0025C) and for the microfluidic chip with either GIF (A=0.0026C) or SMF (A=0.0024C). The absorption spectra (using the supercontinuum source) are plotted for concentrations ranging from 315 µmol/L to 420 µmol/L.

point-of-care diagnosis. The results were therefore repeated by preparing the $Fe(SCN)^{2+}$ solution in artificial saliva.

The results in Fig. 9 show the linearity and comparable absorbance at 480 nm for the $SCN^-$ in water and artificial saliva. This successful demonstration shows that it is possible to extend the tests of these microfluidic chips to saliva, which is a typical biological sample where $SCN^-$ concentrations range from 0.5–2 mM in non-smokers and up to 6 mM in smokers [26]. The limit of detection (LOD) of this simple and practical optofluidic device is determined by the

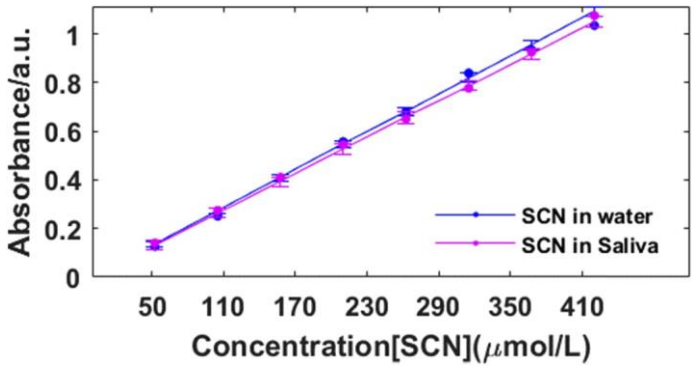


**Fig. 9.** Plot of absorbance at 480nm as a function of $SCN^-$ solution in artificial saliva (A=0.0025C) and in water (A=0.0026C) for the GIF setup.

minimum reliably detected concentration of $SCN^-$ in artificial saliva which is 16.2 µM. Salivary thiocyanate could for instance be used to evaluate the influence of passive smoking on public health or to detect thyroid gland malfunction [22]. Although other techniques exist to detect $SCN^-$ such as surface-enhanced Raman spectroscopy using droplet microfluidic chips [27], and chromatography mass spectroscopy [28], we present a simple and compact fiber-coupled platform to achieve detection, with the technique presented being extendable to cavity-enhanced approaches which would further enhance sensitivity.

# 4. Conclusion

In summary we have demonstrated a microfluidic device which shows identical performance to standard cuvettes for absorption spectroscopy but renders a 10-fold reduction in the sample volume. This is enabled by using graded-index fiber tips which collimate the output of an optical fiber and could allow for longer channel lengths. The GIF tips are shown to allow for a significant reduction in insertion loss when compared with the microfluidic chips using standard SMF. The simple and practical microfluidic chips are shown to detect down to 50 µM concentration of $SCN^-$ in artificial saliva, which is more than sufficient for the quantitative measurement of $SCN^-$ in saliva for the identification of irregularities in saliva and the monitoring of oral health. Moreover, the microfluidic devices demonstrated in this paper could be integrated for lab-on-a-chip devices or implemented for highly sensitive cavity-enhanced absorption technologies.

# Funding

Australian Research Council (IH150100028).

# Acknowledgements

K. Gill, N. Riesen, C. Priest and D. Lancaster acknowledge financial support from ULVAC Inc., and the Australian Research Council Integrated Device for End-User Analysis at Low Levels Research (IDEAL) Hub (IH150100028).

# Disclosures

The authors declare that there are no conflicts of interest related to this article.

# References

1. P. Minzioni, R. Osellame, C. Sada, S. Zhao, F. Omenetto, K. B. Gylfason, T. Haraldsson, Y. Zhang, A. Ozcan, and A. Wax, “Roadmap for optofluidics,” J. Opt. **19**(9), 093003 (2017).
2. C. Song and S. H. Tan, “A Perspective on the Rise of Optofluidics and the Future,” Micromachines **8**(5), 152 (2017).
3. D. Psaltis, S. R. Quake, and C. Yang, “Developing optofluidic technology through the fusion of microfluidics and optics,” Nature **442**(7101), 381–386 (2006).

4. M. Savoini, P. Biagioni, L. Duò, and M. Finazzi, "All-optical subdiffraction multilevel data encoding onto azopolymeric thin films," Opt. Lett. **34**(6), 761–763 (2009).
5. G. Holzner, F. H. Kriel, and C. Priest, "Pillar cuvettes: capillary-filled, microliter quartz cuvettes with microscale path lengths for optical spectroscopy," Anal. Chem. **87**(9), 4757–4764 (2015).
6. F. H. Kriel and C. Priest, "Influence of sample volume and solvent evaporation on absorbance spectroscopy in a microfluidic "pillar-cuvette"," Anal. Sciences **32**, 103–108 (2016).
7. S. R. Neil, C. M. Rushworth, C. Vallance, and S. R. Mackenzie, "Broadband cavity-enhanced absorption spectroscopy for real time, in situ spectral analysis of microfluidic droplets," Lab Chip **11**(23), 3953–3955 (2011).
8. C. M. Rushworth, G. Jones, M. Fischlechner, E. Walton, and H. Morgan, "On-chip cavity-enhanced absorption spectroscopy using a white light-emitting diode and polymer mirrors," Lab Chip **15**(3), 711–717 (2015).
9. A. Nitkowski, L. Chen, and M. J. Lipson, "Cavity-enhanced on-chip absorption spectroscopy using microring resonators," Opt. Express **16**(16), 11930–11936 (2008).
10. S. M. Ball, J. M. Langridge, and R. Jones, "Broadband cavity enhanced absorption spectroscopy using light emitting diodes," Chem. Phys. Lett. **398**(1-3), 68–74 (2004).
11. L. Malic and A. G. Kirk, "Integrated miniaturized optical detection platform for fluorescence and absorption spectroscopy," Sens. Actuators, A **135**(2), 515–524 (2007).
12. C. Wang, Y. Mao, C. Fang, Z. Tang, Y. Yu, and B. Qi, "Analytical method for designing gradient-index fiber probes," Opt. Eng. **50**(9), 094202 (2011).
13. S. Bi, C. Wang, J. Zhu, Z. Yuan, Y. Yu, S. Valyukh, and A. Asundi, "Influence of no-core fiber on the focusing performance of an ultra-small gradient-index fiber probe," Opt. Laser Eng. **107**, 46–53 (2018).
14. D. Lorenser, X. Yang, and D. D. Sampson, "Accurate modeling and design of graded-index fiber probes for optical coherence tomography using the beam propagation method," IEEE Photonics J. **5**(2), 3900015 (2013).
15. M. Zickar, W. Noell, C. Marxer, and N. de Rooij, "MEMS compatible micro-GRIN lenses for fiber to chip coupling of light," Opt. Express **14**(10), 4237–4249 (2006).
16. C. Wang, J. Sun, C. Yang, B. Kuang, D. Fang, and A. Asundi, "Research on a novel Fabry–Perot interferometer model based on the ultra-small gradient-index fiber probe," Sensors **19**(7), 1538 (2019).
17. Y. Zhang, Y. Li, T. Wei, X. Lan, Y. Huang, G. Chen, and H. Xiao, "Fringe visibility enhanced extrinsic Fabry–Perot interferometer using a graded index fiber collimator," IEEE Photonics J. **2**(3), 469–481 (2010).
18. B. Du, X. Xu, J. He, K. Guo, W. Huang, F. Zhang, M. Zhang, and Y. Wang, "In-Fiber collimator-based Fabry-Perot interferometer with enhanced vibration sensitivity," Sensors **19**(2), 435 (2019).
19. N. Riesen, N. Phillips, C. Priest, L. V. Nguyen, and D. Lancaster, "Lensed GRIN fiber-optic Fabry-Perot interferometers," *Frontiers in Optics* JTu7D, JTu7D.4 (2020).
20. J.-Y. Gal, Y. Fovet, and M. Adib-Yadzi, "About a synthetic saliva for in vitro studies," Talanta **53**(6), 1103–1115 (2001).
21. K. Bevziuk, A. Chebotarev, D. Snigur, Y. Bazel, M. Fizer, and V. Sidey, "Spectrophotometric and theoretical studies of the protonation of Allura Red AC and Ponceau 4R," J. Mol. Struct. **1144**, 216–224 (2017).
22. M. F. Erdogan, "Thiocyanate overload and thyroid disease,"˘ Biofactors **19**(3-4), 107–111 (2003).
23. A. Phonchai, T. Srisukpan, S. Riengrojpitak, P. Wilairat, and R. Chantiwas, "Simple and rapid screening of the thiocyanate level in saliva for the identification of smokers and non-smokers by capillary electrophoresis with contactless conductivity detection," Anal. Methods **8**(25), 4983–4990 (2016).

24. K. de Berg, M. Maeder, and S. Clifford, "A new approach to the equilibrium study of iron (III) thiocyanates which accounts for the kinetic instability of the complexes particularly observable under high thiocyanate concentrations," Inorg. Chim. Acta **445**, 155–159 (2016).
25. H. S. Frank and R. L. Oswalt, "The stability and light absorption of the complex ion $FeSCN^{++}$," J. Am. Chem. Soc. **69**(6), 1321–1325 (1947).
26. C. V. Kalburgi, K. L. Naik, M. V. Kokatnur, and S. Warad, "Estimation and correlation of salivary thiocyanate levels in healthy and different forms of tobacco users having chronic periodontitis: A cross-sectional biochemical study," Contemp. Clin. Dent. **5**(2), 182 (2014).
27. L. Wu, Z. Wang, S. Zong, and Y. Cui, "Rapid and reproducible analysis of thiocyanate in real human serum and saliva using a droplet SERS-microfluidic chip," Biosens. Bioelectron. **62**, 13–18 (2014).
28. R. K. Bhandari, R. P. Oda, S. L. Youso, I. Petrikovics, V. S. Bebarta, G. A. Rockwood, and B. A. Logue, "Simultaneous determination of cyanide and thiocyanate in plasma by chemical ionization gas chromatography mass-spectrometry (CI-GC-MS)," Anal. Bioanal. Chem. **404**(8), 2287–2294 (2012).